ABSTRACT

HARDIMAN, CHRISTOPHER MICHAEL. Characterization of the Effect of Radiation Damage on the Thin-Film Stress Behavior of Nanocrystalline 3C SiC. (Under the direction of Dr. Steve Shannon.)

Silicon carbide has attracted a great deal of interest in the field of microelectronics and MEMS due to the enhanced material properties compared to silicon especially for operation in harsh environments. In particular, SiC is well known for its mechanical hardness, chemical inertness, high thermal conductivity, and electrical stability in high temperature and high radiation environments. The degradation of the mechanical properties of SiC due to radiation damage is of particular importance to the fuel performance in next generation high-temperature gas-cooled (HTGC) nuclear reactors which employ SiC as a structural support in response to the high pressures generated due to the release of fission gases. In particular the evolution of the stress characteristics is of particular importance for MEMS and fuel particle applications of thin-film SiC. For all MEMS applications, characterizing the stress behavior of a material is crucial in order to eliminate stress effects such as film cracking and delamination which results from excessively high tensile stress and buckling of structural features which results from excessively high compressive residual stress.

In this project, (111) textured, nanocrystalline 3C-SiC was grown using low-pressure chemical vapor deposition (LPCVD) at a wide range of residual film stresses in order to characterize how the stress gradient evolved with increasing radiation dose. In order to vary the residual film stress the growth pressure was varied while maintaining constant gas flows

and temperature. The film stresses investigated ranged from 673 MPa to -208.667 MPa and were measured after film growth using profilometry to measure wafer curvature.

In order to quantify the stress characteristics on the same dimensional scale as the film, 1 cm x 1 cm dies with four sets of microcantilevers were fabricated and the deflection measured using SEM in order to correlate the deflection to the stress gradient over the thickness of the 3C SiC film. The change in the stress gradient could then be used to monitor macroscopic changes in the 3C film as a result of microstructural changes due to radiation damage. Due to the amorphization of the silicon substrate during irradiation, a second plasma-based process flow needed to be developed and characterized in order to ensure proper release of irradiated microcantilever devices. Pre-irradiation cantilever deflection measurements were made for the film stress values listed above and it was found that the films which had the most compressive residual film stresses exhibited the greatest deflection due to a larger positive stress gradient.

Independent radiation experiments were carried out up to doses of 0.54 dpa using silicon self-ion irradiation at energies of 3 MeV Si^{+} ions and fluences up to 5.5 x 10^{15} ions/cm^{2}. Based on the inverse peak width of the characteristic (111) 3C SiC peak characterized, the dose required for complete amorphization of the engineered, nanocrystalline 3C SiC occurred at around 3 dpa. This was based on GIXRD scans of several different tensile and compressive stressed samples and correlated to high-resolution TEM images. Overall it was found that the radiation tolerance of the engineered nanocrystalline 3C SiC films was an order of magnitude greater than that observed in single crystal 3C SiC.

Characterization of the Effect of Radiation Damage on the Thin-Film Stress Behavior of Nanocrystalline 3C SiC

by
Christopher Michael Hardiman

A thesis submitted to the Graduate Faculty of
North Carolina State University
in partial fulfillment of the
requirements for the degree of
Master of Science

Nuclear Engineering

Raleigh, North Carolina

2013

APPROVED BY:

_____	_____
Dr. Steven Shannon Committee Chair	Dr. Jacob Eapen Committee Member
_____	
Dr. Jon-Paul Maria Committee Member	

DEDICATION

I would like to dedicate this to my mother Teresa, step-father Mark, and my father Jeff who have both helped me every step of the way and been an incredibly important part of my life. Without their sacrifices, constant encouragement, patience, and pressure this would not have been possible. I would also like to dedicate this to my brother Matt, his wife Lauren, and my little niece Kyndal for constantly being there for me.

BIOGRAPHY

Christopher Michael Hardiman was born in Huntsville, AL on February 20th, 1982 to Teresa and Jeff Hardiman. He is one of two sons and has a younger brother named Matt Hardiman. With his father Jeff being in U.S. Navy he moved around quite a lot, including living in Scotland for three years. After attending Escambia High School in Pensacola, FL for two years, he moved with his mother to Gastonia, NC where he attended and graduated South Point High School in Belmont, NC. In the summer of 2008 after several years of underachieving he finally achieved his Bachelor of Science degree in Nuclear Engineering from North Carolina State University. Following this he spent a year and a half in the Post-Bachelor Studies (PBS) program at North Carolina State University earning his way into graduate school under the direction of a huge influence, Dr. Steve Shannon.

ACKNOWLEDGEMENTS

There are several people who have devoted their time to assist me, gave me a great deal of knowledge and are of the highest caliber people I have ever known. I am very grateful for the extensive training and patient assistance of Marcio Cerullo, Nicole Hedges, Henry Taylor, Dave Vallenga, and Bruce Sprague of the NCSU Nanofabrication Facility. The same is true of the industry users of the facility who devoted valuable time and energy in helping a struggling graduate student when they had no obligation to do so. They have taught me so much during my time working in the facility and this would not have been possible without them. I am also very thankful for the invaluable help of Chuck Mooney, Dale Batchelor, and the entire staff of the Analytical Instrumentation Facility (AIF). I am also very grateful to Dr. Jon-Paul Maria, Dr. James Lebeau, Dr. Yi Liu, Christopher Shelton, Adedapo Oni, and Bahar Alipour of the Materials Science & Engineering Department for their time and invaluable help. I would also like to take the faculty and staff, past and present, of the Nuclear Engineering Department for their patience and for the opportunity I have been given. A special thanks to Matthew Cabral for his help with this project. I would also like give a very special thanks to my advisor and friend Dr. Steve Shannon for giving me an opportunity and believing in me.

Funding for this project was provided by the Department of Energy Nuclear Energy University Partnership grant number 10-817. I am very grateful for the support of the DOE NEUP program for the duration of this project.

TABLE OF CONTENTS

LIST OF TABLES

LIST OF FIGURES

CHAPTER 1: Introduction & Motivation

Silicon carbide has attracted a great deal of interest in the field of microelectronics and MEMS due to the enhanced material properties compared to silicon especially for operation in harsh environments. In particular, SiC is well known for its mechanical hardness, chemical inertness, high thermal conductivity, and electrical stability in high temperature and high radiation environments. [MEH1] The degradation of the mechanical properties of SiC due to radiation damage is of particular importance to the fuel performance in next generation high-temperature gas-cooled (HTGC) nuclear reactors which employ SiC as a structural support in response to the high pressures generated due to the release of fission gases. The TRISO fuel particle utilizes the SiC layer due to its high density and high tensile strength as shown below in Figure 1.1.

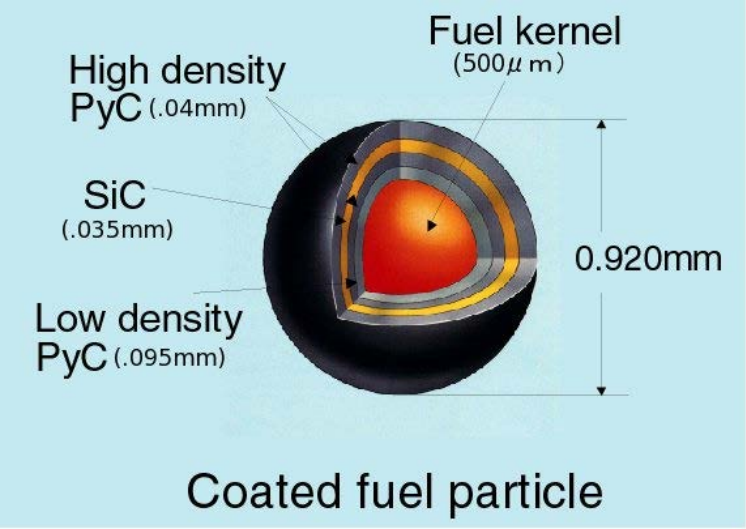

Figure 1.1: Illustration of TRISO Fuel Particle. [PET]

Microcracking due to radiation-induced stress changes of thin film SiC is of particular importance to the fuel efficiency of next generation nuclear reactors. David Petti of the Advanced Gas Reactor (AGR) Program reported stress values ranging from -700 MPa to 450 MPa with a more concentrated tensile stress distribution for fuel particles that had undergone cracking of the porous PyC layer during neutron irradiation and a more uniform compressive stress distribution for uncracked particles. [PET] The uncracked particles showed a stress distribution that ranged from -700 MPa to -600 MPa as a function of SiC layer thickness. These two stress distributions are shown below in Figure 1.2.

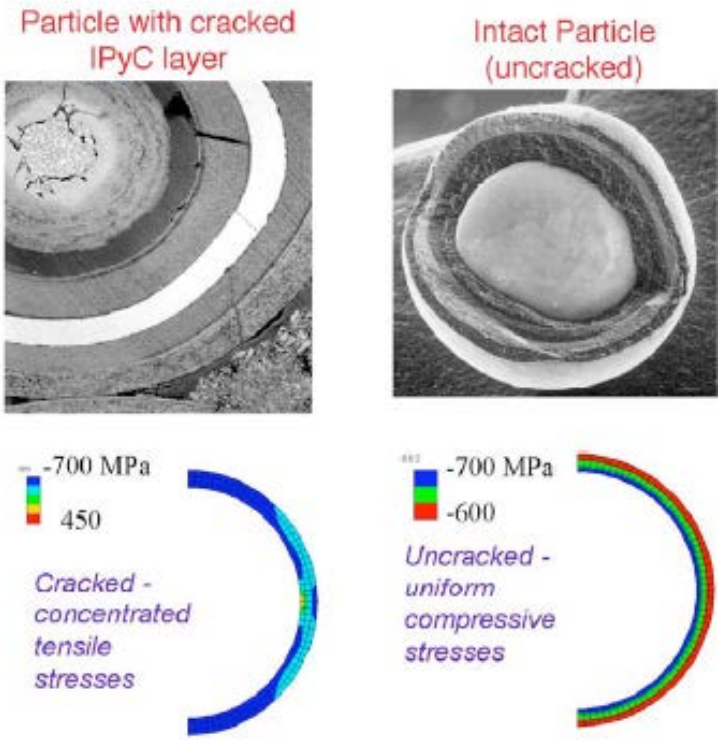

Figure 1.2: Difference in stress distribution of SiC structural layer of cracked and uncracked fuel particles. [PET]

From Figure 1.2 that the TRISO particle with the cracked PyC layer has a more concentrated tensile stress gradient in the structural SiC layer at the apex, whereas for the particle with the intact PyC exhibits a more uniform change in stress over the SiC film thickness and is purely compressive in nature.

The stress behavior of thin-film polycrystalline 3C SiC as a result of radiation damage is also of great importance in the area of harsh environment MEMS such as instrumentation applications in the aerospace industry which requires a stable, high-temperature, and radiation resistant material for solid-state sensors and satellite systems. For all MEMS applications, characterizing the stress behavior of a material is crucial in order to eliminate stress effects such as film cracking and delamination which results from excessively high tensile stress and buckling of structural features which results from excessively high compressive residual stress. [FU3]

The aim of this project is to characterize the effects of displacive radiation, specifically ion bombardment, on the microstructural and residual film stress behavior of LPCVD-deposited, thin-film, polycrystalline 3C SiC. Damage formation, defect clustering, and lattice disordering caused by the ionizing radiation results in a degradation of the crystallinity and thus changes properties such as electrical performance, thermal conductivity, and mechanical properties as a result. In addition irradiation-produced defects can exceed a critical strain level above which the crystal becomes amorphous. The crystalline-to-amorphous (c-a) transition of single-crystal 3C SiC has been shown to be a strong function of temperature and radiation dose. This project focuses on the 3C SiC polytype in polycrystalline form.

In this project a methodology was developed for varying the residual stress in thin-film polycrystalline 3C SiC by varying the pressure of the LPCVD growth process. A stress matrix was created in order to observe if the stress response to radiation damage had any dependence on the initial stress state over a range of stress states. The residual stress states grown fall within the range simulated for the TRISO fuel particle by Petti et al. and serve as a suitable range to continue the investigation of SiC as a radiation tolerant structural material. A method of fabricating arrays of microcantilevers was developed in order to measure the stress gradient of the thin-film SiC pre- and post-irradiation. By measuring the deflection of the microcantilevers before and after the introduction of microstructural damage as a result of ion bombardment, the stress behavior could be quantified based on direct measurement.

Advances in growth techniques of SiC and the compatibility with well known silicon processing techniques has generated new opportunities for replacing silicon as the material of choice especially in microelectromechanical systems (MEMS). The desire for this replacement is due to the superior mechanical and electrical properties of SiC. One of the most promising polytypes of SiC, especially for use in harsh environment microelectromechanical systems (MEMS) applications is the cubic-structured, polycrystalline 3C SiC. Several methods have been researched for growing 3C SiC including plasma-enhanced chemical vapor deposition (PECVD), ion-beam assisted deposition (IBAD), and atmospheric pressure chemical vapor deposition (APCVD), and low-pressure chemical vapor deposition (LPCVD).

Silicon carbide can exist is several types of crystal orientations exhibiting a one-dimensional polymorphism called polytypism. Each of the polytypes, of which more than

250 exist, are distinguished by different stacking arrangements of the identical, closed-packed planes of bonded Si and C atoms, referred to as Si-C double layers.[SNE, MEH2] These Si-C layers can be visualized as a plane of Si atoms coupled with a plane of C atoms and the stacking of the successive Si-C double layers occurs along the basal plane with a direction along the c-axis and normal to the Si-C double layer plane. [SNE, MEH2] Although there is such a large number of polytypes, SiC can only exist as three different crystal systems: cubic, hexagonal, and rhombohedral.[CHE1] The stacking order of the covalently bonded Si-C double layers and the crystal structure uniquely describes the SiC polytype. The most commonly used and manufactured SiC polytypes are 3C, 4H, and 6H. The number corresponds to the number of non-repeating Si-C stacking sequences in the unit cell and the adjacent letter describes the crystal structure of the polytype. A schematic representation of the 3C SiC or β-SiC unit cell and stacking sequence is shown below in Figure 1.3.

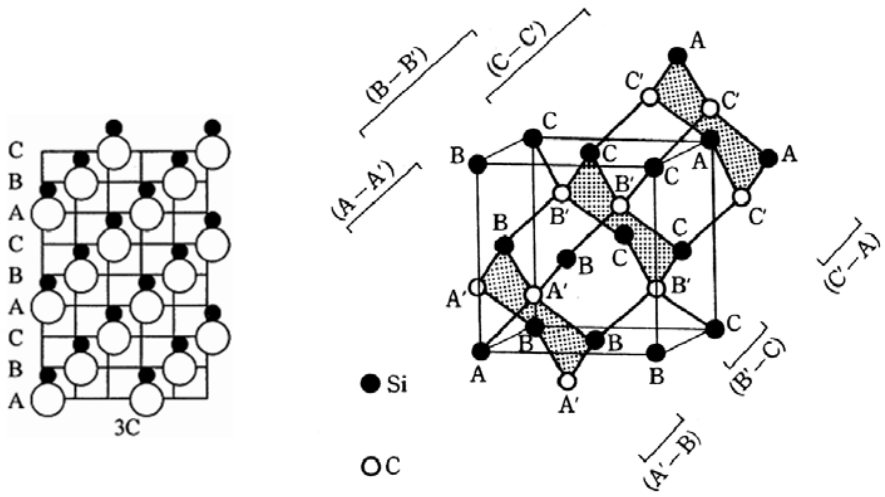

Figure 1.3: Crystal structure and stacking sequence of 3C SiC [SNE]

3C SiC has the only cubic symmetry out of all the known polytypes of SiC. Although so many SiC polytypes exist, the stability of them is dependent on temperature primarily, but impurities which can cause a deviation in the Si:C stoichiometry has been shown to have a part in SiC polytype instability.[SNE,MEH2] The phase diagram shown below in Figure 1.4 illustrates the various states of SiC in general as function of both temperature & atomic ratio of Si:C.

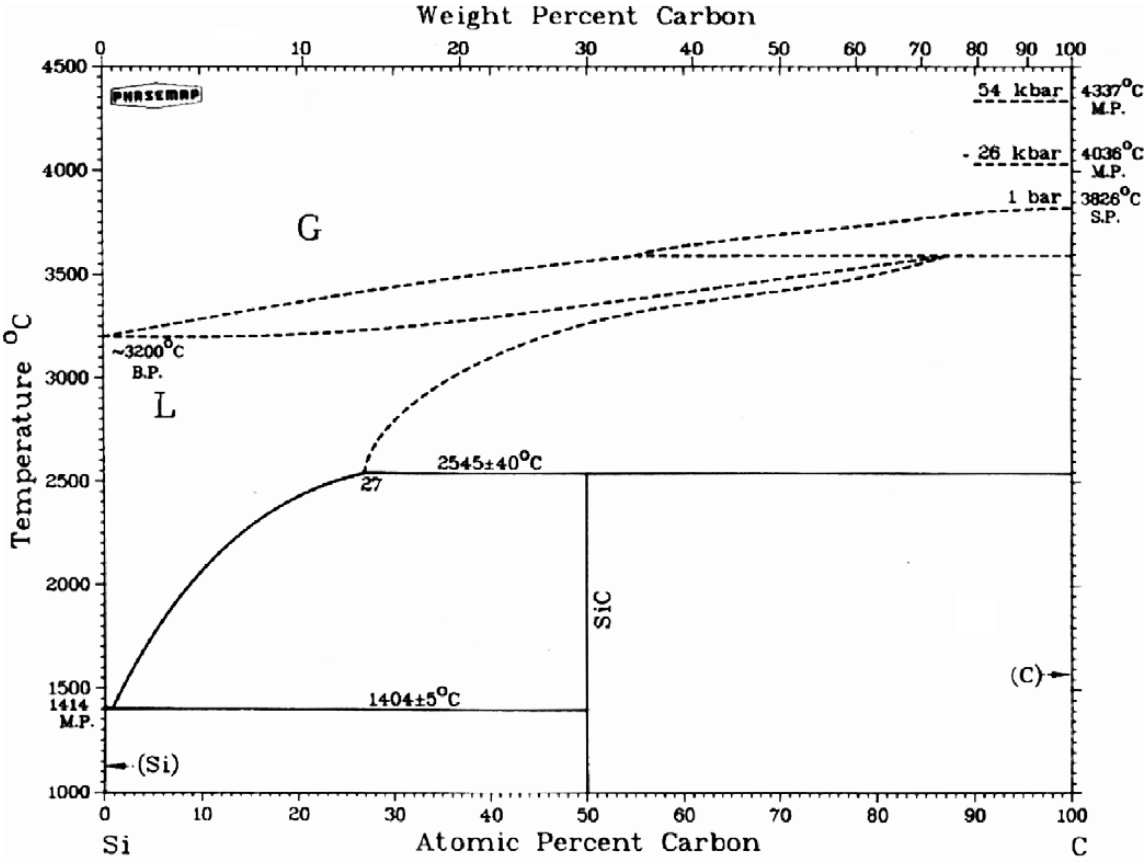

Figure 1.4: Phase diagram of SiC depicting temperature as a function of atomic ratio of Si:C. [SNE]

It is apparent from Figure 1.4 that the thermal stability of SiC decreases with decreasing carbon atomic percent. For stoichiometric SiC, the material is stable up to a temperature of approximately 2500 °C.

The accepted material properties of the 3C SiC polytype grown in this project is shown below in Table 1.1.

Table 1.1: List of representative 3C SiC material properties.

Property	***Value***
Maximum Operating Temperature (°C)	~2500
Thermal Conductivity (W/cm-K)	3.6 @ 300 K
Thermal Expansion Coefficient (10^{-6} °C)	4.2
Young's Modulus (GPa)	448
Band Gap (eV)	2.4
Breakdown Field (MV/cm)	4
Poisson Ratio[SNE]	0.21

The most important of these for the purpose of stress characterization is the Young's modulus and Poisson ratio in determining the biaxial modulus and residual film stress based on wafer curvature methods as discussed later in this report. For instance, the relation between the biaxial stress and strain for an isotropic thin film can be represented in terms of Young's Modulus and the Poisson ratio by the following equation:

$$\sigma = \frac{E}{1-\nu}\varepsilon \qquad \text{Eq.1}$$

Through this relation the stress characteristics can be directly related to the dimensional changes caused by strain in the microstructure.

CHAPTER 2: 3C SiC Growth

2.1 Introduction to CVD & Thin Film Growth

Chemical vapor deposition (CVD) involves the process of chemically reacting volatile compounds which contain the desired constituents that make up the film with other gases in order to produce a nonvolatile solid which deposits atomistically on a substrate. One thing that makes CVD so unique is that the controllable growth of films with varying stoichiometry is possible. [OHR] The governing mechanisms of any CVD process can be divided into the following stages: introduction of chemically reactive gaseous species into the reactor, diffusion of the reactants to the substrate, adsorption of the reactants on the substrate, chemical reaction of the reactant and the substrate, and the desorption and gaseous transport of any reaction by-products out of the reactor. This process is shown graphically in Figure 2.1 below.

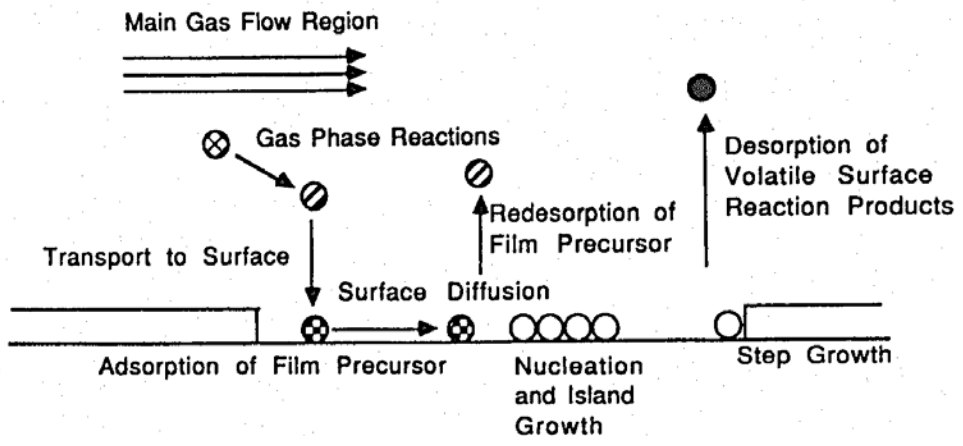

Figure 2.1: Graphical representation of the processes involved in CVD film growth. [MAD]

The most important consideration of any CVD process is the thermodynamic feasibility of the chemical reaction between the reactants and the substrate. This is determined by the Gibbs free energy as shown below in Eq.1,

$$\Delta G = \Delta H - T\Delta S \qquad \text{Eq.1}$$

where ΔH is the difference in enthalpy between the products and the reactants including desorbed by-products, T is the process temperature, and ΔS is the difference in entrophy between the products and reactants. For a given reaction, the individual change in free energy of a particular molecular species is given in terms of the change in enthalpy and entropy at STP and at the process pressure and temperature conditions. For the reaction specific to the experimental growth method used in this project the reactants consisted of dichlorosilane (SiH_2Cl_2) and acetylene (C_2H_2) with hydrogen acting as the carrier gas. Based on Eq.1, using the Shomate Equation and ΔH and ΔS values from the NIST chemical database, the overall Gibbs free energy for the reaction of the experimental LPCVD process is -64.6891 kJ/mol. This implies that the SiC formation is thermodynamically feasible and spontaneous.

The manner in which a thin-film grows depends on several growth process factors such as pressure, substrate temperature, the ratio of the individual reactants introduced, and the substrate on which the thin-film is grown. Regardless of the material being grown, the progression of thin-film formation involves stages of nucleation and growth. The beginning stages of film growth occur when a sufficient number of the reactant vapor atoms/molecules condense on the substrate. This is known as nucleation and after enough atoms have bonded together, small clusters or islands are formed. [OHR] These islands are highly mobile and

as adatoms impinge on the small clusters, the islands grow in size and the density of islands on the substrate increases rapidly. The collection of smaller clusters and subsequent merging of the islands occurs by a process of coalescence, which ultimately decreases the island density by forming a connected network of larger islands between which denuded zones exist. The isolated denuded zones are free of condensed reactant atoms and thus further nucleation can occur. With further deposition, these denuded zones fill in and shrink due to coalescence and the process proceeds until a continuous layer exists.

There are three accepted modes regarding thin-film nucleation and growth for CVD processes: Volmer-Weber, Frank-Van der Merwe, and Stranski-Krastanov. In the Volmer-Weber model nucleation of the film occurs in the form of discrete 3D nuclei on the surface of the substrate. The film growth progresses by an increase in both the number and size of the present nuclei. This increases until the nuclei intergrow with each other to form a continuous film. In the Frank and Van der Merwe model, film growth tends to proceed in a layer-by-layer growth. This is due to the fact that adatoms are more likely to attach to the substrate surface than to other film material surfaces [FRE]. Once small islands are formed, additional adatoms form on the periphery of the islands where they can bond directly to both the substrate and film atoms. This process proceeds by subsequent epitaxial growth. The Stransky-Krastanov model combines features of the two previous models. Nucleation and growth occurs in a layer-by-layer manner until a finite number of monolayers are produced. Subsequent film formation occurs by the formation of discrete nuclei as described by the Volmer-Weber model. [HAR, FRE] A pictorial representation of these different modes is shown below in Figure 2.2.

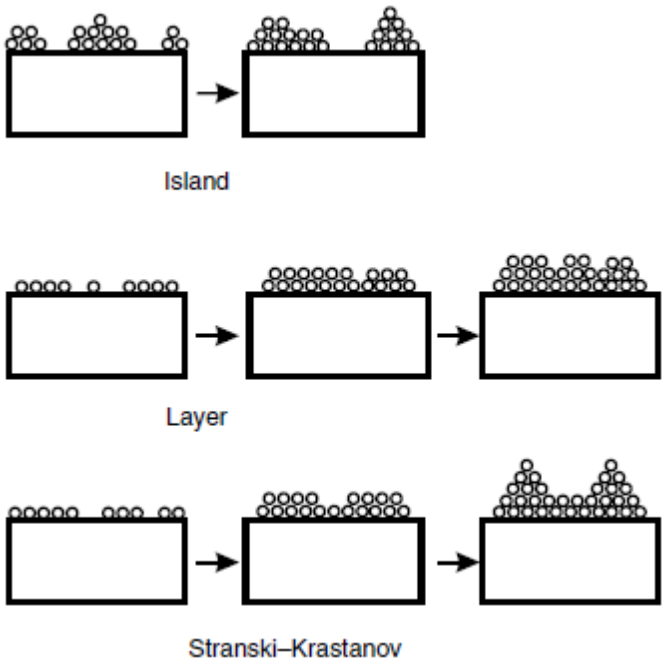

Figure 2.2: Modes of Thin-Film Growth. [HAR]

2.2 Review of Common SiC Growth Techniques

Silicon carbide is only just beginning to become a widespread substitute for Si as the semiconductor material of choice due in no small part to issues regarding the deposition of SiC films. For most MEMS applications Si/polysilicon films can be grown on a mass production scale using relatively low temperatures and simple resistive heating furnaces. SiC presents a greater challenge due to its structure. When heteroepitaxially growing SiC on Si the resulting thermal mismatch results in residual stresses of the SiC film [2,6] as is the case when growing any thin-film material heteroepitaxially. One material property of SiC that is very promising for applications to MEMS also poses a considerable problem for deposition of SiC, with that being the thermodynamic stability of SiC at very high temperatures. This

makes the use of an annealing process to eliminate the residual stresses impractical. [CHE1] The only practical method in reducing the film stress of the SiC film is to adjust certain parameters in the furnace process being used to grow thin-film material.

Considering doping of SiC for use in semiconductor devices, the diffusion constants are all very low making solid source diffusion impossible so doping of SiC is typically achieved using ion implantation or the more commonly used in-situ doping. [CHE1] However, despite these issues several techniques have been developed for growing the three most relevant polytypes: 3C, 4H, and 6H. 3C SiC has emerged as the polytype of choice in MEMS applications because it can be heteroepitaxially grown on Si which is readily available. The two hexagonal polytypes form at temperatures above the melting point of Si making synthesis on Si wafers impossible. [CHE1] However, 6H SiC pressure and acceleration sensors have been fabricated by growing epitaxial 6H films on commercially available 6H SiC wafers using CVD furnace processes similar to those commonly used in the fabrication of Si devices. [CHE1] Due to the preference of 3C SiC in MEMS applications the following discussion of various deposition techniques is geared toward the 3C polytype.

Atmospheric Pressure Chemical Vapor Deposition (APCVD) was one of the first techniques used to grow epitaxial 3C and 6H SiC films mainly because this method has fewer components that are sensitive to temperature than low-pressure systems. This is advantageous for SiC epitaxy since typical temperatures range from approximately 900 to 1300 °C for the growth of 3C films on Si substrates to over 1700 °C for 6H growth on 6H SiC substrates. [CHE1] In general, APCVD reaction chambers consist of a double walled fused silica tube which has chilled water running between the walls. Maintaining a low

temperature on the chamber walls acts to minimize deposition, as well as any particulate formation. [CHE1] These systems can be either orientated horizontally or vertically, with the latter being useful for larger wafer sizes and can also serve to minimize particulate deposition on the substrate due to the vertical orientation of the wafer. A schematic of a typical horizontal APCVD system is shown below in Figure 2.3. To achieve the high temperatures for deposition needed in order for epitaxial growth, the substrates are loaded onto a susceptor which is coated with SiC. This SiC coated, graphite piece is placed central in the chamber with respect to the RF-driven induction coils wound around the chamber. This susceptor is heated by the RF coils through induction to the elevated temperatures required for SiC CVD growth.

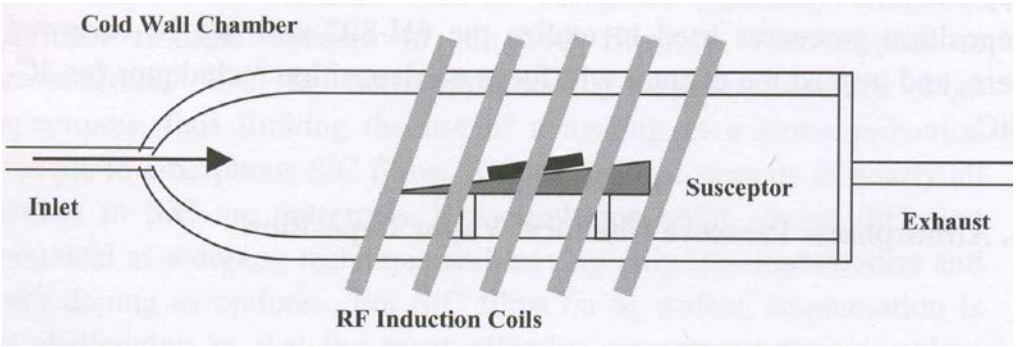

Figure 2.3: Schematic of Typical APCVD Chamber Used for SiC Epitaxy [CHE1].

The most common APCVD process for growing 3C SiC on Si involves exposing the Si wafer to a hydrocarbon gas mixed with an H_2 carrier gas and heating the susceptor to roughly 1300 °C. The most common of the hydrocarbon gases used in this type of process is propane (C_3H_8). Over about a 90 second period, the gas flow and temperature control is held constant

during which a process known as carbonization occurs. The carbonization process consists of the propane gas flowing over the heated sample where it is decomposed into reactive hydrocarbon radicals. These radicals readily react with the free Si atoms to form a thin layer of SiC. [ROY2] This process alone is not the sole means of growing the 3C SiC films because the growth rates tend to be nonlinear, dropping off with time. [CHE1, ROY2] To produce the several micron thicknesses used in MEMS applications, the growth rate is increased by the addition of a gas containing Si, typically silane (SiH_4) into the carrier gas. [CHE1, ROY2] This process is not limited to epitaxial growth of SiC and a similar process has been created to grow polycrystalline, 3C SiC films. [ROY2] Poly-SiC films have been shown to be more versatile in MEMS applications because they can be grown on several different substrates i.e. SiO_2, polysilicon, and Si_3N_4. [CHE1] The process for growing Poly-SiC varies with the substrate, but if the substrate is amorphous then a carbonization stage is not very effective and the susceptor is heated to a temperature slightly lower than that for heteroepitaxial 3C SiC growth and the precursor gases are injected [CHE1].

Another important growth technique used in SiC MEMS fabrication is plasma-enhanced chemical vapor deposition (PECVD). PECVD enables SiC films to be formed at much lower temperatures than APCVD in the range of just 200-400 °C. Typically the microstructure of as-deposited PECVD SiC films is amorphous but crystalline SiC films can be achieved by a post-growth anneal [CHE1]. PECVD SiC is particularly useful because it can be deposited using commercially available PECVD systems due to its amorphous nature. Typical precursor gases used in PECVD processes include SiH_4, CH_4, and $C_6H_{18}Si_2$. With the latter, hexamethyldislane, being a single precursor feed gas. The low operating

temperature is due to the process being controlled by the electron temperature, T_e, of the plasma.

Perhaps the most widely used method of SiC film growth, however, is low pressure chemical vapor deposition (LPCVD). This process allows for a wide range of precursors to be used and due to the low processing pressure film thicknesses tend to be more uniform than the previously mentioned APCVD method [CHE1]. For epitaxial 3C SiC growth, several processes exist using both single and dual precursors. Processes involving single precursors can be used for epitaxial 3C growth without a need for a carbonization stage and at lower temperatures than APCVD and dual precursor LPCVD processes. [CHE1] One such process which is useful in the development of free-standing 3C SiC membranes for sensors involves the use of mono-methylsilane ($H_3Si\text{-}CH_3$) which yielded 3C SiC films on Si substrates at temperatures as low as 1000 °C. [CHE1] An example of dual precursors used in the epitaxial growth of 3C SiC involved the use of dichlorosilane or DCS (SiH_2Cl_2) and acetylene (C_2H_2) over a much lower temperature range of 750-1050 °C with the maximum temperature corresponding to the film growth steps. Using a multiple step process which involved an initial carbonization stage, the DCS and acetylene flows were alternated such that the first step involved the deposition of a thin Si epitaxial layer and the second carbon-based precursor carbonized the Si layer producing a SiC epitaxial film [CHE1].

LPCVD is also widely used to deposit polycrystalline 3C SiC films, which is quickly becoming the dominant crystalline phase in SiC MEMS. Since the growth of poly-SiC films does not require an initial carbonization step prior to film growth, LPCVD growth of polycrystalline 3C SiC only requires that the precursors dissociate and react at a specified

substrate temperature. Both single and dual precursors can be used for the growth of poly-3C SiC. An example of a LPCVD system designed for high volume production of poly-3C SiC is shown on the following page in Figure 2.4. This process involves the use of the dual precursors DCS and acetylene and can deposit MEMS quality poly-3C SiC films at temperatures ranging from 750-900 °C and pressures from 460 mTorr to 5 Torr [CHE1].

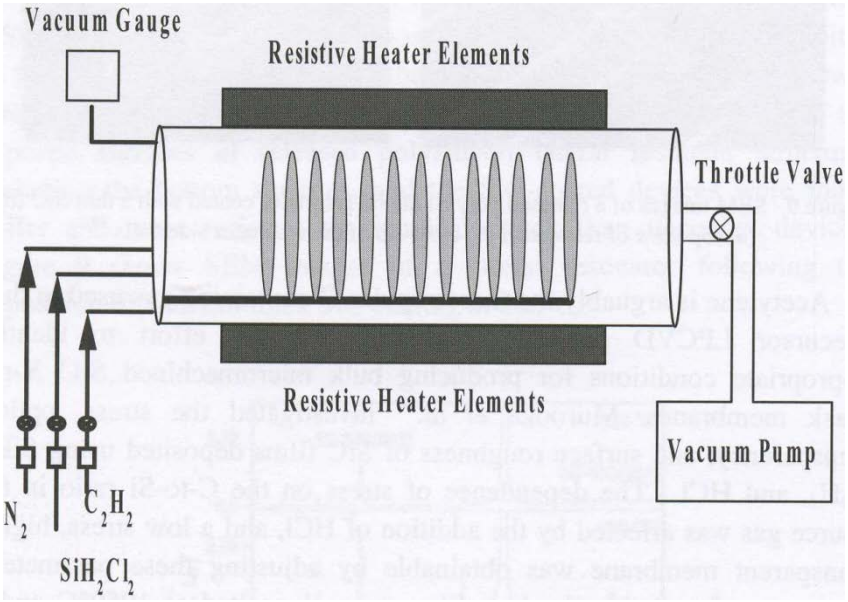

Figure 2.4: Schematic of LPCVD System Used for High-Volume Production of 3C SiC. [CHE1]

A wide variety of deposition techniques have been developed for MEMS grade SiC films, with the most widely used and well characterized being CVD. The most commonly characterized polytype for deposition is 3C SiC since it is the only polytype which can be grown on Si. This makes it the most widely used for MEMS applications. Processes exist using the previous CVD techniques discussed that can deposit single crystalline,

polycrystalline, and amorphous SiC films which are of the quality suitable for MEMS and micromachining.

2.3 Experimental 3C SiC Growth Process

Advances in growth techniques of SiC and the compatibility with well known silicon processing techniques has generated new opportunities for replacing silicon as the material of choice especially in microelectromechanical systems (MEMS). The desire to do so is due to the superior mechanical and electrical properties of SiC. One of the most promising polytypes of SiC for use in MEMS is the cubic-structured, polycrystalline 3C SiC. Several methods have been researched for growing 3C SiC including plasma-enhanced chemical vapor deposition (PECVD), ion-beam assisted deposition (IBAD), and atmospheric pressure chemical vapor deposition (APCVD) but the most well characterized method is low-pressure chemical vapor deposition (LPCVD). The process used to grow the 3C SiC is similar to already reported LPCVD processes discussed previously. The poly-SiC films were deposited on 100 mm diameter (100) silicon wafers in a high-throughput, hot-wall, horizontal furnace using the dual precursor gases dicholorsilane (SiH_2Cl_2) and acetylene (C_2H_2) as the supply of silicon and carbon. In order to produce semiconductor-grade poly-SiC films, ammonia was incorporated to introduce nitrogen as an in-situ n-type dopant in order to study the effects of radiation on electrical performance. In most of the runs made, the ammonia gas flow was minimal in order to grow thin-films for mechanical characterization. However, since the characterization involved an already established baseline process, the gas flow parameters were held constant and a 7 sccm NH_3 flow was present for each undoped run.

The dual-precursor gases were introduced into the cylindrical reaction chamber simultaneously following an initial carbonization stage in which an ultra-thin carbon film was deposited on the silicon substrate. The purpose of the initial carbon film is to promote stoichiometry and to improve the uniformity of the SiC films. [MAD, SER] The gas flow rates during the main deposition step of the process were held constant for the duration. The temperature of the LPCVD process was also constant and was maintained along the length of the quartz tube at 900 °C. Figure 2.5 shown below depicts the LPCVD process used with temperature as a function of time.

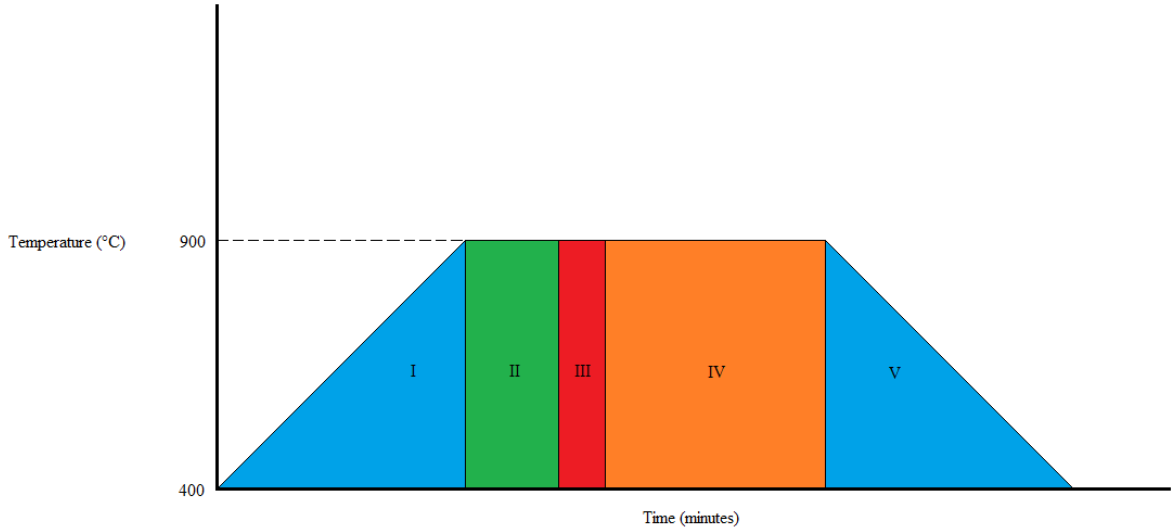

Figure 2.5: Visual summary of LPCVD process steps used in poly-SiC growth.

As shown in Figure 2.5 the LPCVD process used to grow our poly-SiC thin-films was achieved at a constant temperature of 900 °C. The initial step of the LPCVD process (I) represents a ramp-up stage for the heating coils in the furnace tube for which the ambient

temperature varied between 400 and 424 °C. Step II involved a temperature stabilization to eliminate any deviation and nonuniformity of the temperature measured at the back, center, and front of the quartz tube. In addition, this step included an N_2 purge where a maximum nitrogen flow was introduced in order to automatically adjust the throttle valve position to the predetermined growth process pressure. The carbonization of the silicon substrate was conducted in step III and involved a two-minute flow of C_2H_2 mixed with a hydrogen carrier gas. Step IV in Figure 2.5 represents the bulk growth step of the 3C SiC thin-film. The time of the main deposition stage depends exclusively on the deposition pressure and the desired thickness. This is due to the fact that the process pressure was found to directly affect the deposition rate as is shown below in Figure 2.6.

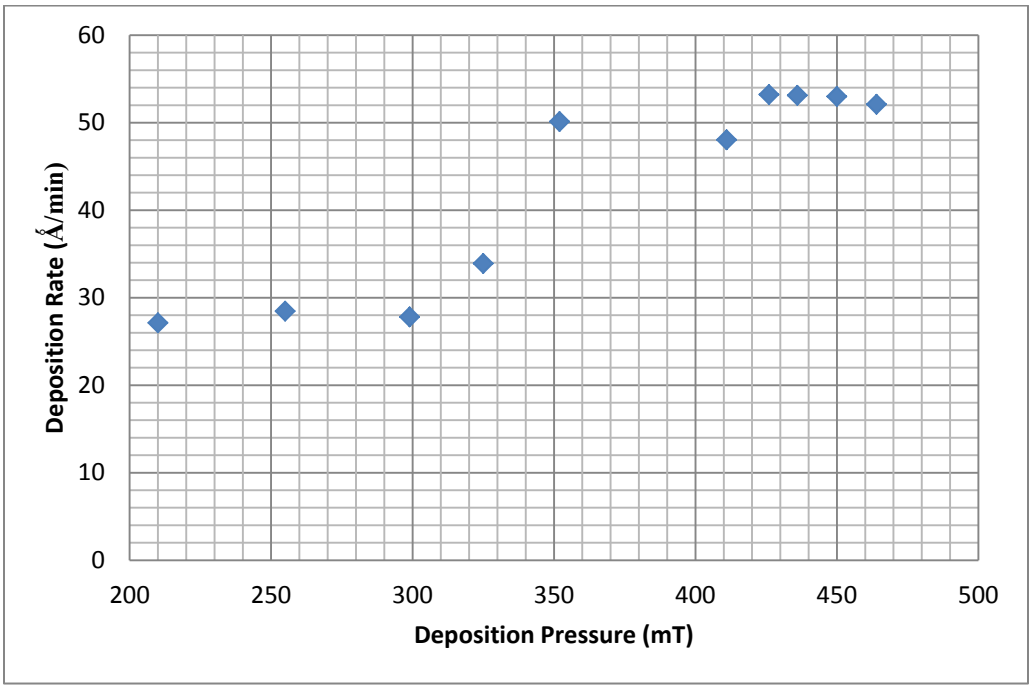

Figure 2.6: Experimentally measured SiC growth rate as a function of LPCVD process pressure for undoped 3C SiC.

All deposition rates were determined for the wafer that corresponded to the middle position with respect to the other wafers in the run. Typically each run consisted of 3-4 wafers in all. The deposition rates were found to be consistent across the small section of the quartz boat. It is important to note that the undoped 3C SiC thin-films grown using this process included a small amount of ammonia since the undoped films were run with the baseline process on the LPCVD furnace. From Figure 8 above, it is apparent that a nearly linear increase in the deposition rate occurs around the transition from tensile to compressive residual stress. This coincides with the transition from lower to higher process pressure which occurs around 400 mTorr.

CHAPTER 3: Stress Characterization & Analysis

3.1 Residual Stress in Thin-Films

A common concern for materials used in the fabrication of MEMS structures is residual stress and stress gradient in thin-films. It has been reported in literature that poly-SiC films deposited on silicon substrates generally exhibit high residual stress and stress gradients. [FU3] For MEMS applications, the residual stress and stress gradients can be highly detrimental to the performance of MEM devices. For instance, highly tensile stresses can result in deformation of the active structures and highly compressive stresses can lead to buckling of clamped structures. Residual stress gradients can also result in deflection of cantilever structures that is out-of-plane. While the effects of high residual stress are undesirable in MEMS application, they are the basis of this report as an effective method of determining the change in the stress characteristics of the thin-film SiC as a result of radiation damage.

Stress in thin films is divided into two categories: intrinsic and extrinsic stresses. Intrinsic or growth stresses are strongly dependent on the mobility of adatoms on the growth surface and the mobility of the grain boundaries during growth [FRE1], as well as the homologous temperature (T_{sub}/T_{melt}). The main source of extrinsic stress for the growth of nanocrystalline 3C-SiC on Si is the difference in the thermal expansion coefficient (~8%) which results in the external loading as a result of the post-growth temperature change. This effect is constant and repeatable provided the substrate and film thicknesses are consistent.

Therefore understanding the development of the intrinsic stress is an important aspect since it can be directly controlled through adjustment of the growth parameters.

It is first important to understand the nature of the measureable effect of residual stresses present in film-substrate systems. The initial assumptions are that the film and substrate are represented as two thin plates, each of which have different lateral dimensions, and that the thickness of the film is much smaller than that of the substrate. [OHR] Following the adhesion of the film to the substrate, the film seeks to recover its previous lateral dimensions and this in turn causes the substrate to deform to reach a new equilibrium state. The actual bending occurs due to the presence of bending moments at the edges of the film-substrate stack. The induced strain on the substrate caused by the thin-film seeking to return to its original geometry is due to several stress mechanisms which for polycrystalline films are thermal and intrinsic in nature. A pictorial representation of this is shown below in Figure 3.1.

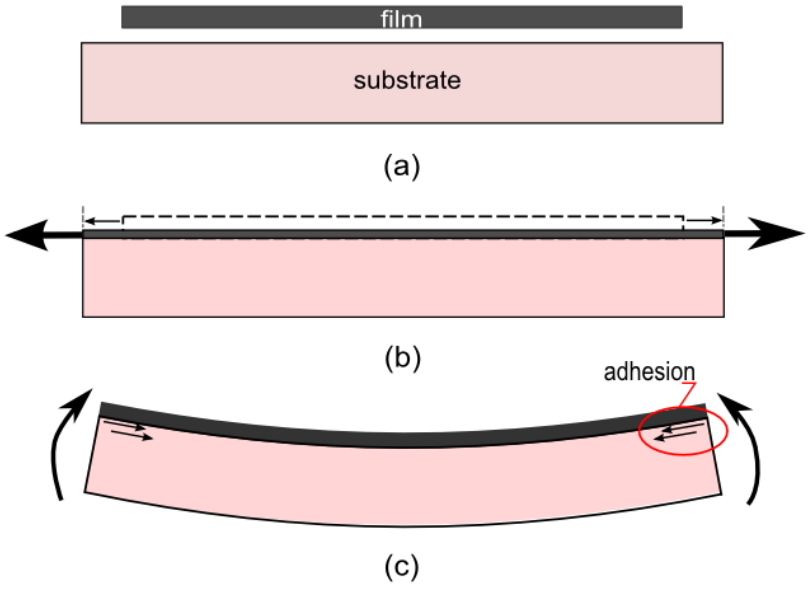

Figure 3.1: Sequential Stages of deposition of thin-film on substrate. (a) Initially the substrate is unstrained (b) deposited film is strained to match substrate and (c) film-substrate stack is deformed until equilibrium is reached. [CAR]

The cause of the strain induced matching of the thin-film to the substrate is predominantly caused by lattice mismatching for single-crystal SiC. This is caused by the ~22% difference in the lattice constants of SiC and Si. In poly-SiC this is due to the mismatch (~8%) of the thermal expansion coefficients as well as intrinsic, microstructure strain as a result of defects such as stacking faults and twins and the nature of the grain growth and the evolution of the grain structure. [YUN] Regardless of the cause the measureable response of residual stress is general, a film which is stretched to match the surface area of the substrate will generate uncompensated bending moments at the edges which will bend the substrate upwards and result in a residual tensile stress state in the thin-film and vice versa for a film which has a compressive stress state. [OHR] The bending is ultimately the result of counterbalancing the

bending moments that are generated as a result of the deformation induced. These thermal and intrinsic strain mechanisms are superimposed as a total residual stress in the film which was measured using mechanical profilometry and quantified using the Stoney relation. This approximation of film stress is given below in Eq. 2,

$$\sigma_f = \frac{1}{6R}\frac{E_s d_s^2}{(1-\nu_s)d_f} \qquad \text{Eq. 2}$$

where R is the radius of curvature of the thin-film/substrate, E_s is Young's modulus of the substrate, d_s is the thickness of the substrate, d_f is the thickness of the film, and v_s is the Poisson ratio of the substrate. A more accurate model, especially for the 3C SiC films discussed in this report includes the contribution of thermally induced strain on the extent of bowing and is shown below in Eq. 3.

$$\frac{1}{R} = \frac{6E_f(1-\nu_s)}{E_s(1-\nu_f)}\frac{d_f}{d_s^2}(\alpha_s - \alpha_f)\Delta T \qquad \text{Eq. 3}$$

In the above equation, α_s and α_f are the thermal expansion coefficients of the substrate and film, respectively and ΔT is the difference between the temperature of the growth process and room temperature. [OHR] This deflection is based on a thermal stress addition to the Stoney relation which is shown below in Eq. 4,

$$\sigma_f(T) = (\alpha_s - \alpha_f)\Delta T\frac{E_f}{(1-\nu_f)} \qquad \text{Eq. 4}$$

There are some assumptions in determining residual film stress by using the Stoney formula which affects the accuracy of this model. This method assumes that substrate deflections are initially small for all dimensions, which is a reasonable assumption since the initial silicon

wafers are relatively flat. This is evident by the pre-deposition scans taken for a typical run made while creating the stress matrix and is shown below in Figure 3.2. All curvature measurements were made at three standard angles and the stress is determined using a built in algorithm based on Eq. 2. It is apparent that the curvature of the wafer depicted in Figure 10 from the change in the curvature after the heteroepitaxial growth of the SiC, the internal stress of the silicon wafer is low. A second assumption made by the Stoney relation is that both the film and substrate material properties are homogeneous and isotropic. [CAR] This is not quite accurate as the difference in the maximum and the average stress in some runs was found to be over 100 MPa.

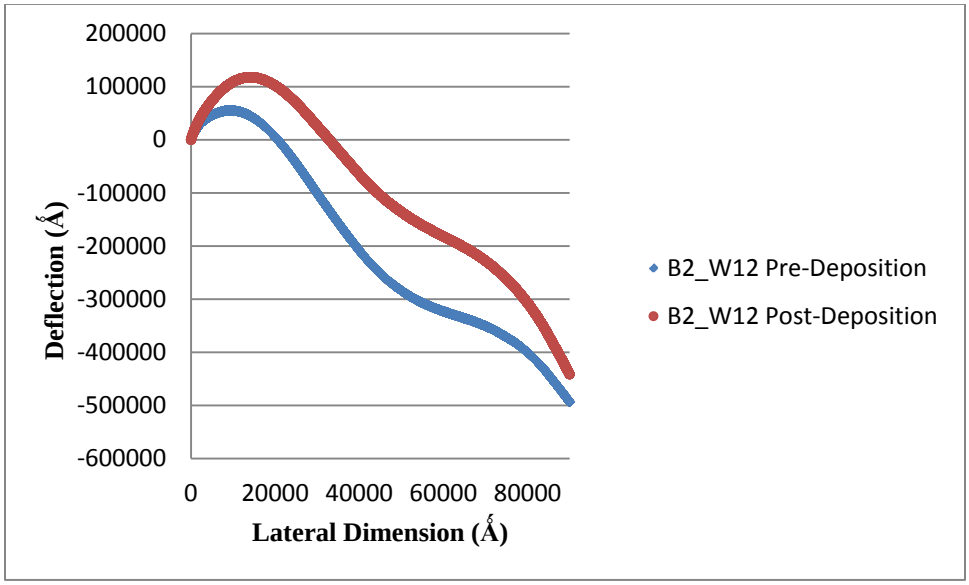

Figure 3.2: Sample Pre- and Post-deposition profilometry scan of a compressive stress run.

3.2 Residual Stress & Film Analysis

In order to control the residual stress state of the thin films, the deposition pressure was adjusted between 210 and 475 mTorr. Adjusting pressure as a means of controlling film stress was previously reported by Fu, et al. [FU3] Fu and his colleagues presented a general trend of increasing compressive thin film stress state with increasing deposition pressure, however further increases in deposition pressure resulted in a saturation at -98 MPa. That same observation was made in this work as well, albeit at a much lower pressure.

The method used in the analysis of the residual film stress consisted of using a stylus-type profilometer to measure the wafer curvature at three angles relative to the major flat of the (100) Si wafer. Of these three scan angles one was perpendicular to the main flat and one parallel to the main flat. The curvature of the silicon wafers were measured before and after deposition and a stress was determined based on Eq. 2. The stress values from the three scan angles were then averaged in order to get a single value for the residual stress. Shown below in Figure 3.3, is the experimental data of residual film stress as a function of process pressure for wafers located in the center of the range of slots used in the furnace boat. The purpose of using a small range of slots was due to the observed stress variation with respect to wafer position along the length of the furnace tube.

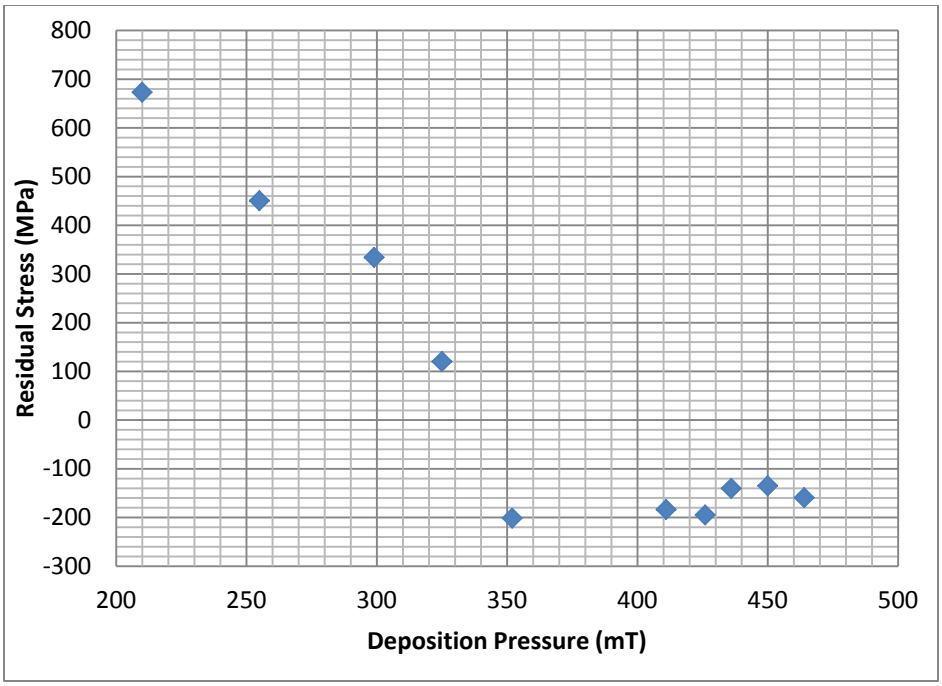

Figure 3.3: Film stress behavior as a function of LPCVD process pressure.

A possible explanation of this behavior involves the difference in the grain sizes observed at low and high pressure states. [FU3] These are directly impacted by the LPCVD process parameters and general geometry of the reactor chamber. In addition, the residual stress has also been attributed to the grain formation at the film-substrate interface. It has been observed that for highly compressive 3C SiC films the grains are more aligned suggesting that the lateral growth of grains is limited during the initial stages of nucleation. [FU3] This observation has been attributed to the high density of nuclei present at the surface due to the higher process pressure. The high deposition pressures result in non-preferential grain growth and grain crowding. The opposite is observed for tensile films grown at lower pressures.

For most film-substrate combinations, with a high growth flux and moderate homologous temperature (T_{sub}/T_{melt}) polycrystalline films are grown by the Volmer-Weber (VW) mode. [FRE1] The adatoms form clusters on the substrate which increase in size until they impinge on adjacent clusters to ultimately form a continuous film. Stress changes in the polycrystalline film correlate with the sequential steps in the film growth process. This is represented below in Figure 3.4.

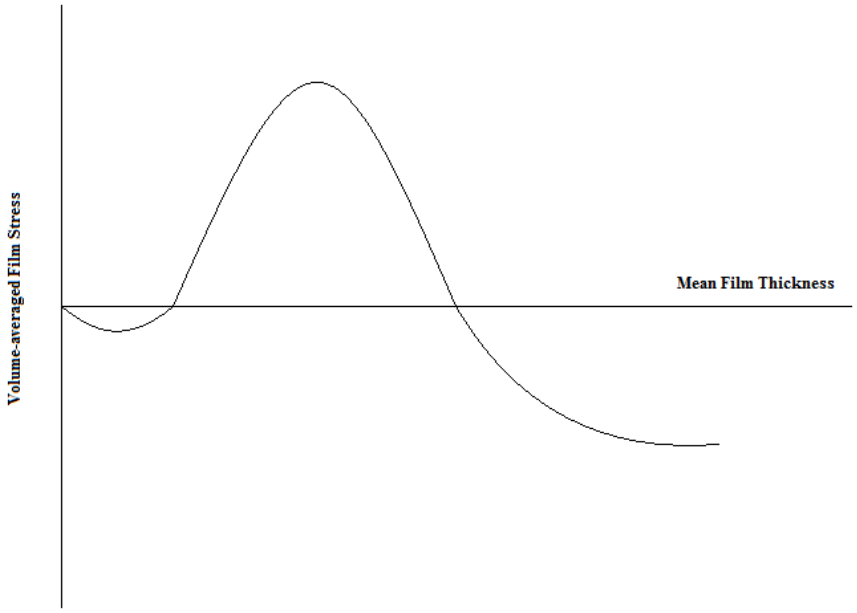

Figure 3.4: Qualitative volume averaged residual film stress behavior as a function of sequential growth steps for polycrystalline thin film growth. [FRE]

The initial compressive film stress observed in the growth of many polycrystalline thin films corresponds to the early stage of island growth. During the island growth process, the crystallites forming on the growth surface become "attached" to the substrate such that

upon further growth of the islands an internal elastic strain is generated. Normally this strain would relax as the radius of the island increased but due to the constraint of the substrate this internal relaxation does not occur. [FRE1] As a result of the increasing strain due to the increase in the size of island a volume-averaged compressive stress results in the individual crystallites. A second contributing factor is the importance of the density of the islands present on the growth surface. The stress field of an isolated island has no resultant force on the substrate and the magnitude of the field tails off within a short distance from the island. For a distribution of islands to result in a non-negligible stress field, the density of the islands must such that the fields of the islands interact. [FRE1]

This small overall compressive film stress is active until the islands establish large area contiguity or island-to-island coalescence across the substrate. As mentioned previously, this stage of the growth process adatoms continue to impinge on the islands and as a result the surface area of the islands expand until they begin to merge together. During this process the volume-averaged film stress becomes highly tensile. The most widely accepted explanation of this compressive to tensile transition during the initial stages of polycrystalline film growth is based on work performed by Hoffman and Doljack and later by Nix. [CAP, FRE1] They hypothesized that the small gaps between impinging islands can be closed by forming grain boundaries. As the islands begin to make contact they still have a relatively high surface area and therefore a high surface energy. As the islands continue to coalesce and the grain boundary is formed, the decrease in the surface area and therefore the high surface energy is replaced by the relatively low interfacial energy of the grain boundary. In lowering the net total energy of the system of islands and the corresponding reduction in

surface area of the film, the participating islands become elastically strained with a tensile state. [FRE1] The critical island size at which coalescence occurs is generally influenced by a combination of process parameters such as the growth flux (function of pressure), substrate temperature, and surface diffusivity of the impinging adatoms. [FRE1]

The final evolution in the stress behavior shown in Figure 3.4 occurs with continued film growth and is represented by a transition from tensile to a steady-state compressive stress state for a fixed growth flux and substrate temperature. [FRE1] The compressive stress that arises in polycrystalline films has been attributed to the excess number of atoms in the film due to the deposition flux and the presence of grain boundaries. [CHA, FRE1] The supersaturated distribution of adatoms on the growing film provided by the growth flux have free energies greater than the surface atoms of the growing film, which have free energies higher than atoms in the interior of the film. The free energy of the surface atoms may not be sufficient to drive the incoming adatoms into interstitial sites in the lattice, but the surface atoms can lower their free energies by migrating into the grain boundaries. [FRE1] This incorporation of excess atoms into the grain boundaries results in a compressive stress in the film. In addition the driving force for adding additional atoms into the grain boundaries decreases with increasing magnitude of the compressive stress, which leads to the steady-state value observed in the experimental data shown in Figure 3.3.

The high tensile stress states at lower process pressures can potentially be explained by the reduction of grain boundary area and corresponding grain growth. This coincides with the larger grain sizes observed in the 3C SiC films. This effect is a result of the fact that the material inside the grain boundaries is less dense than inside the grain due to the relative

atomic disorder inside the grain boundaries. Therefore a reduction in the grain boundary area leads to a densification of the film and tensile stresses in it. [FRE] An energy per unit area is associated with each grain boundary surface which is representative of the amount of excess energy of the grain boundary above that of the lattice structure within the grains. [FRE1] This excess energy can be reduced by decreasing the total area of the grain boundary surface, which is equivalent to a reduction of the net length of the grain boundary surface as measured parallel to the film-substrate interface. For a representative material sample with several interior grain boundaries, the material undergoes a stress-free isotropic contractive strain when the grain boundary surface area is reduced. [FRE1] However, since the material is constrained against normal displacement due to the surrounding bulk material an elastic extensional strain is induced. This elastic strain corresponds to an elastic energy with increases parabolically with increasing grain boundary area reduction. [FRE1] The degree with which the elastic energy changes with respect to grain boundary area reduction is based on the amount and nature of the initial stress state of the material. [FRE1] If it is assumed that an initial compressive stress state exists, then the critical grain size at which the free energy of the system is at a minimum increases, thereby promoting a greater degree of grain growth and a larger resulting tensile stress. [FRE1]

Is it has been observed that the columnar grains present in the 3C SiC films exhibit highly textured (111) orientation observed by transmission electron microscopy (TEM) and X-ray diffraction (XRD) analysis. Columnar grains are formed if one crystal orientation is preferred during film growth. The initial distribution of grain orientations is random, but those grains with their preferred growth orientation parallel to the film normal dominate over

the inclined grains during growth competition. Once the columnar microstructure has evolved, adatoms can immediately add to the fast-growing crystalline planes without inducing any compression. The preferred crystal orientations with the fastest growth rates are the {111} directions as is evident by the highly textured <111> grain orientation. As a consequence of the preferred growth direction, any new incoming adatom may deposit itself in the grain boundary region between two grains. Even though this will cause an increase in the strain energy, it may be the lowest overall energy state for the adatom. [GAO1] The crystallinity of the 3C SiC films does not exhibit a large difference when analyzed at different residual stress conditions, as is shown below in Figure 3.5.

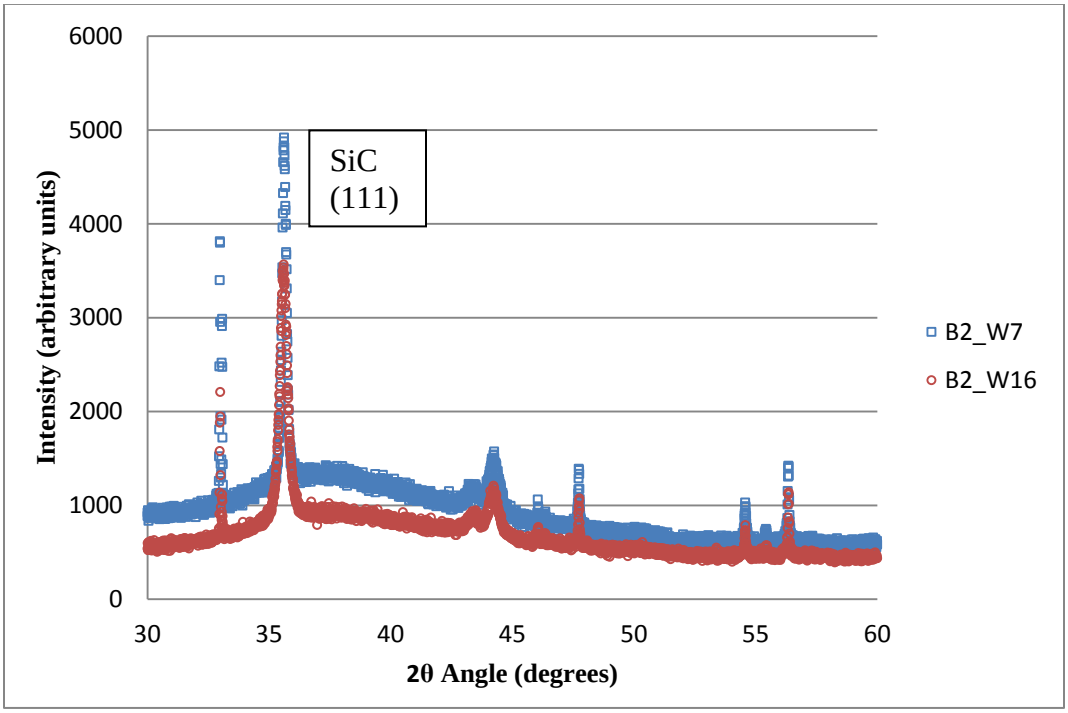

Figure 3.5: θ-2θ scan results for highly tensile and compressive stressed 3C SiC films.

Shown below in Figure 3.6 is a glancing incident angle XRD (GIXRD) scan made of the compressive stress sample B2_W16 shown in Figure 3.5. By changing the tilt angle, ω, with respect to the exact 2θ angle location of the characteristic (111) 3C peak the primary silicon peak and reflection peaks which tends to obscure lower intensity SiC peaks can be eliminated. GIXRD essentially tilts the sample stage such that the x-rays interact with the thin-film only. Such scans were performed on a variety of stress states in collaboration with colleagues at the University of Tennessee-Knoxville in order to determine critical irradiation dose which is discussed later in this report.

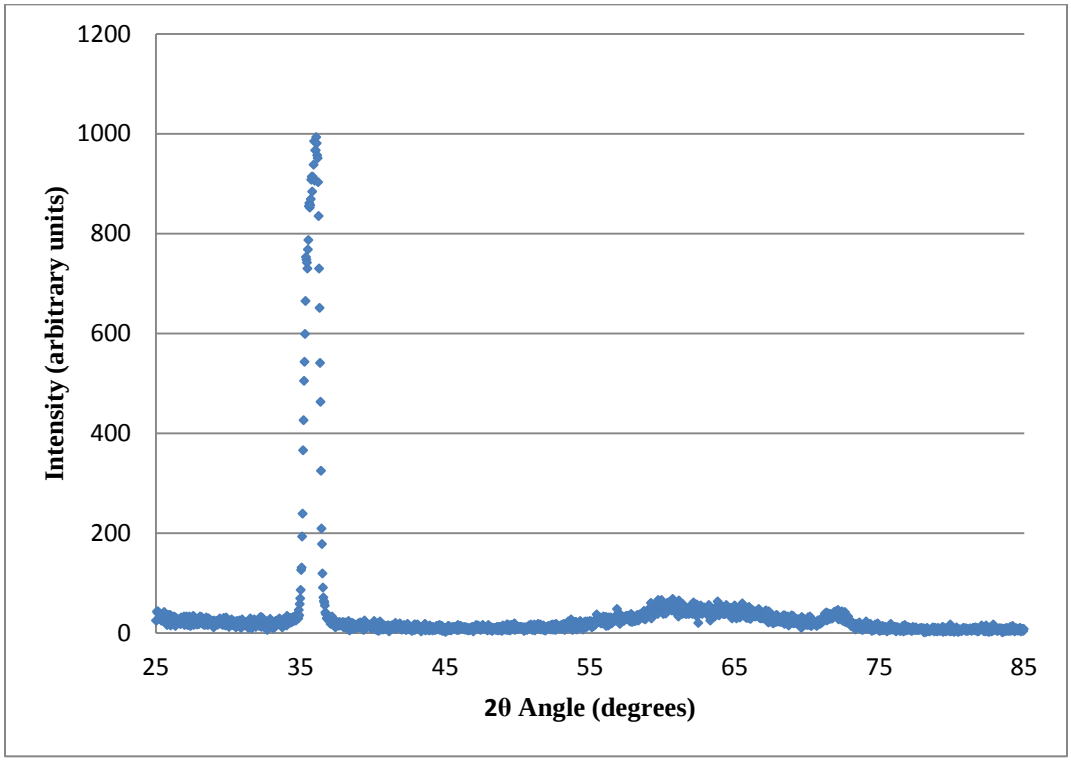

Figure 3.6: GIXRD of 3C SiC thin-film deposited at approximately 300 mTorr.

The peak at around 35° is the characteristic (111) 3C peak and there is some indication of another orientation perhaps either (311) located at around 71.7° or (222) located at around 75°.

The following TEM images, shown in Figure 3.7, exhibit the qualitative observation mentioned above showing that the films grown at higher pressures exhibit smaller grain widths than those films grown at lower pressures.

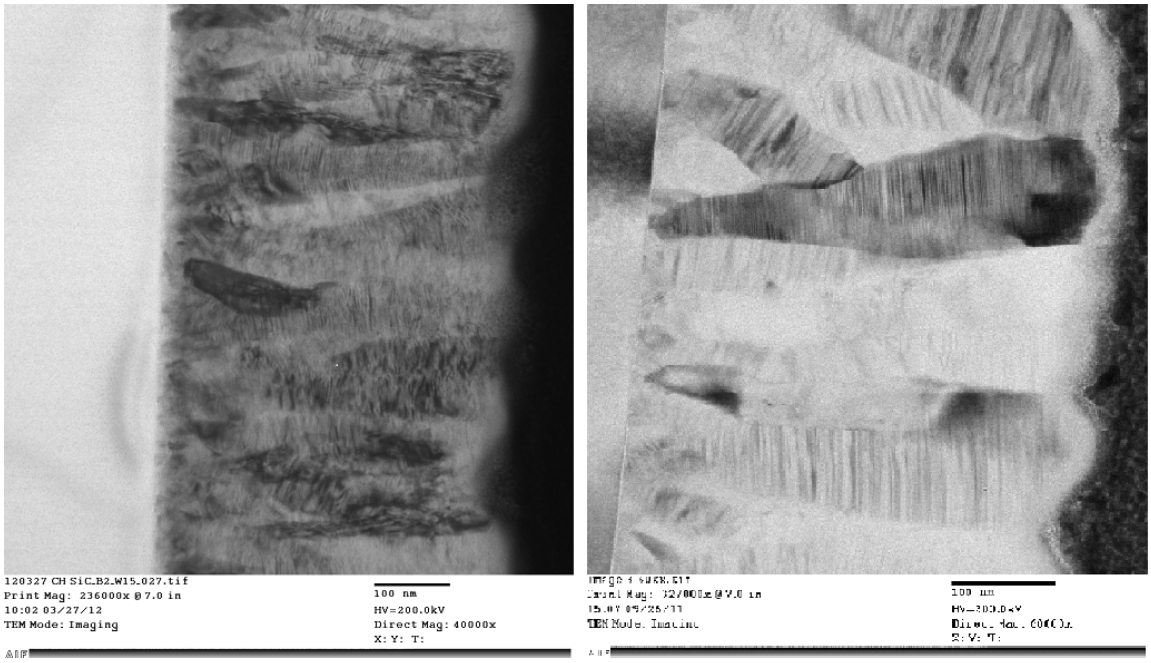

Figure 3.7: TEM images depicting smaller lateral growth of grain boundaries and higher degree of uniform orientation of left image (highly compressive film) compared to the right image (highly tensile film).

In order to characterize the change in the residual stress-strain characteristics of the varied stressed 3C SiC films due to the onset of radiation-induced lattice damage it was necessary to develop a platform which provided a means to quantify changes in the stress

characteristics and in the crystallinity and microstructure of the film. This was achieved by using arrays of dies containing adjacent microcantilevers and open areas of 3C SiC which were utilized for focused ion beam (FIB) material removal for transmission electron microscopy (TEM) and XRD. TEM and XRD were used to analyze the microstructure of the film which is discussed below.

The polycrystalline 3C SiC films grown experimentally contain large densities of stacking faults (SFs) within the individual grains. Stacking faults are defects in which the proper order of stacking planes is interrupted by the addition of an extra plane due to misoriented islands in the LPCVD growth. [SER] These errors in stacking sequences occur along the (111) and are the result of the island growth method common to heteroepitaxy. [YUN] The formation of these SFs is believed to be dominated by atomic deposition errors on the {111} planes of individual crystallites and mismatches of lattice sites during the coalescence of islands during film growth. [YUN] It has been proposed that these SFs attribute to higher radiation tolerance observed in the nanocrystalline SiC. [ZHA2] In order to attempt to control the SF density, the carbonization pressure was changed with respect to the main growth pressure. This idea was based on previous research conducted on single-crystal epitaxial growth of 3C SiC conducted by A. Severino, et al. where the pressure difference between carbonization processes using LPCVD and APCVD systems was investigated. Although the temperatures they used were much higher than 900°C, controlling the growth pressure of the initial carbon seed layer seemed to be a logical first attempt. Shown below in Table 3.1 are the run conditions used in these initial test runs.

Table 3.1: Summary of growth pressures for LPCVD runs to control SF densities

Experiment #	***Carbonization Pressure (mTorr)***	***Main Growth Pressure (mTorr)***
1	231	264
2	418	434
3	330	330
4	248	444
5	434	225

The two runs investigated using high-resolution TEM are samples from the last two entries in Table 3.1. The approximate SF densities were determined to range from 0.058-0.288 nm^{-2} for the run where the carbonization pressure was 248 mT compared to the growth pressure of 444 mT and 0.3891-0.6159 nm^{-2} for the carbonization pressure of 434 mT compared to the growth pressure of 225 mT. Shown below in Figure 3.8 are high-resolution TEM images of the samples used to estimate the SF densities.

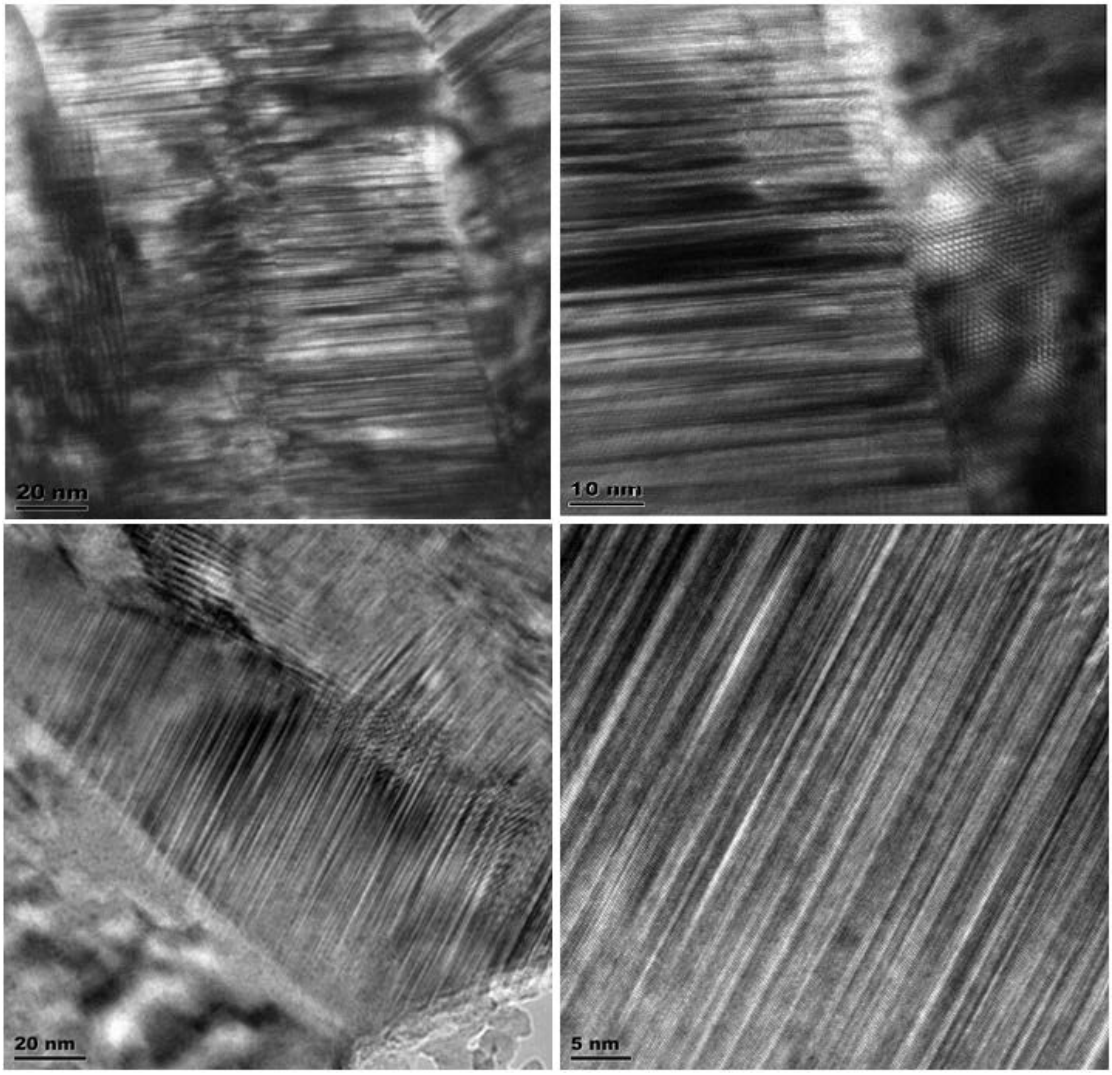

Figure 3.8: High-resolution TEM images of samples from experiments 4 and 5, discussed above, illustrating the difference in microstructure. (Top) Images correspond to 248 mT carbonization/444 mT growth; (Bottom) images correspond to 434 mT carbonization/225 mT growth.

In the images shown in Figure 3.8, an apparent lamellar structure within the grains is consistent in the 3C films grown, regardless of growth process parameters. Also apparent in

Figure 3.8 is the mixing of SFs with those of adjacent grains. This is evident by the interference in the images known as Moire fringes.

3.3 Microcantilever Design Process

The cantilever is an ideal structure to characterize the internal stress of the 3C SiC since if a cantilever under fixed-free conditions and made of a homogenous material would have no intrinsic stress-induced bending if the intrinsic stress is uniformly distributed throughout the film thickness. As a result any nonuniformity in the stress distribution throughout the thickness of the film would cause a gradient in the stress. The gradient in the stress gives rise to bending of the cantilever after release from the substrate and is a direct indication of the intrinsic stress gradient of the 3C SiC film.

Two process designs were developed to fabricate the microcantilever devices with the difference between the two approaches being based on the method used to release the SiC cantilever beams from the silicon substrate. The initial approach involved etching the silicon substrate using a potassium-hydroxide (KOH) anisotropic chemical etch but due to etch difficulties with post-irradiated samples and stress-induced delamination a purely plasma-based approach was needed. The need for a plasma-based process flow was also due to an oversight in the initial photolithographic mask design as discussed at the end of this section.

The mask design was based on a design used by Liudi Jiang et al. who used this design in order to analyze the resonance characteristics of 3C-SiC for microsensor applications. [JIA1] The anchors serve to eliminate any torsional component of beam deflection. In the mask design process it was important to incorporate microcantilever devices across the entire wafer to account for spatial film thickness and stress variations.

Shown below in Figure 3.9 is a schematic of the photolithography mask used for pattern transfer of the cantilever design onto the wafer. Each die consists of two sets of four cantilevers with open areas adjacent to each set. This is enables a direct comparison of adjacent sets of cantilevers for pre- and post-irradiation.

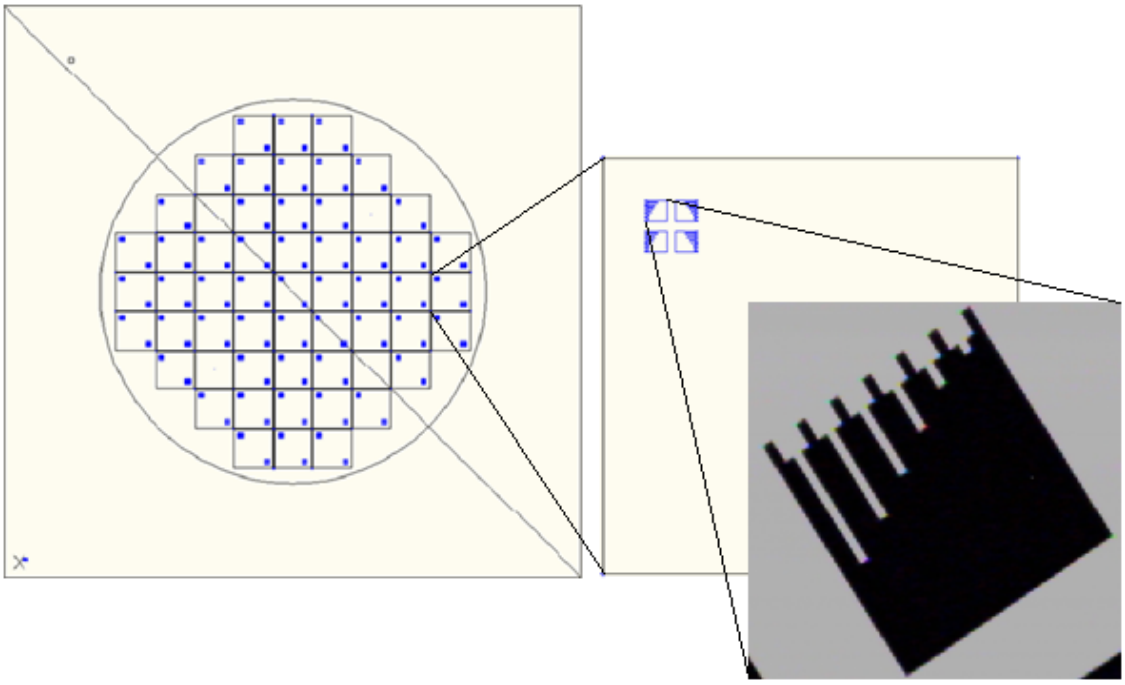

Figure 3.9: 1st level photolithography mask layout.

At various points in both design processes, plasma etching was employed using two common industrial plasma sources: capacitively-coupled and inductively-coupled. A typical capacitively-coupled plasma (CCP) source consists of two electrodes (cathode and anode) with the plasma acting as the dielectric. A schematic representing a typical CCP system is shown below in Figure 3.10.

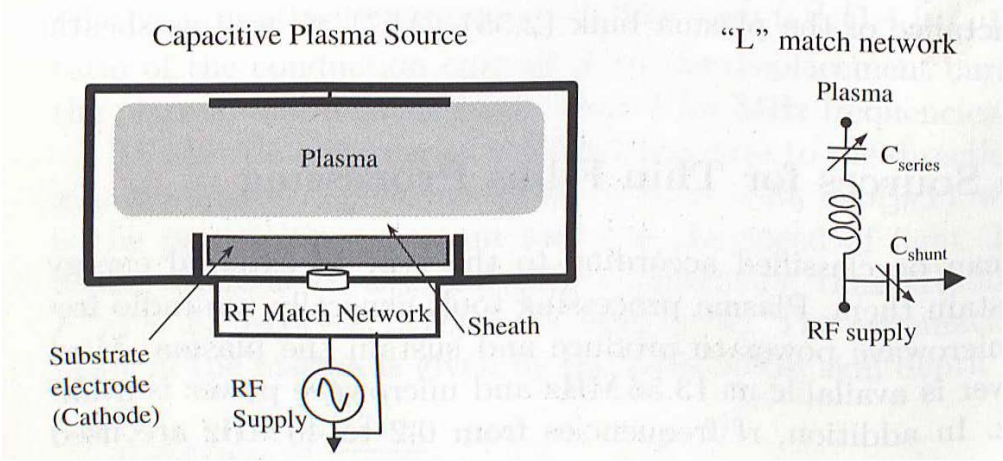

Figure 3.10: Typical capacitively-coupled plasma (CCP) source. [SHU]

Typical CCP systems involve an RF-powered cathode, on which the substrate sits, that is operated at the standard RF frequency of 13.56 MHz. These systems produce low density plasmas (~10^{16} m^{-3}) and use high voltages on the powered electrode necessary to achieve dc bias voltages to yield fast etching through energetic ion bombardment. [COB]

In inductively-coupled plasma (ICP) systems the plasma is formed by coupling the applied RF current delivered by way of RF coils wound parallel to a dielectric wall through induction. The dielectric wall also serves to reduce the need of capacitive coupling allowing low accelerating DC-bias voltages across the sheaths. [LIE] A diagram of a typical ICP plasma source is shown below in Figure 3.11.

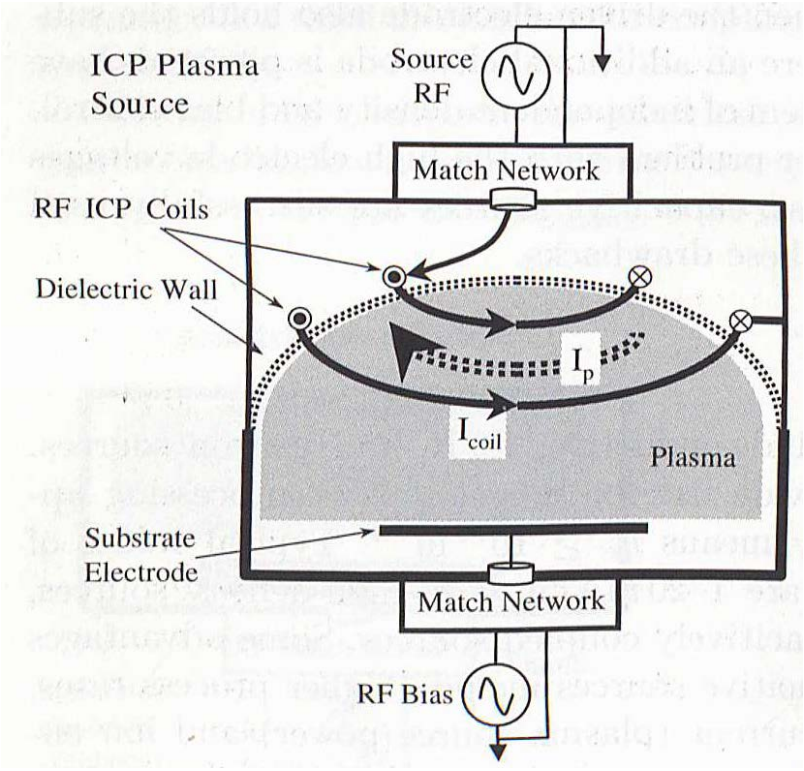

Figure 3.11: Typical inductively-coupled plasma (ICP) source. [SHU]

The RF current induce opposing RF current in the plasma concentrated within a skin depth of the plasma surface. The induced current is carried primarily by thermal electrons through ohmic heating by rapidly transferring power by electron-electron and electron-neutral collisions. Power is also transferred by a collisionless heating process in which free electrons in the bulk plasma interact with the oscillating inductive electric fields within the skin depth layer. [LIE] The inductive RF coils are commonly driven at the standard 13.56 MHz using a 50-Ω supply matched using a L-shaped matching network which uses variable series and shunt capacitors. In order to control the ion energies striking the substrate, the substrate is typically placed on a second powered electrode (RF bias supply).

The preliminary analysis prior to the first step of the cantilever fabrication process involves the use of profilometry to measure wafer curvature after SiC growth and determine the residual film stress. Following the determination of the stress, a 200 nm aluminum thin film is deposited on the SiC to serve as a hard mask for subsequent plasma etching and the structural layer for the first level photolithography. The deposition of the aluminum film was achieved by the thermal evaporation of 99.99% pure aluminum pellets placed on a tantalum crucible which is placed in physical contact with two separate electrodes. The largest concern during the evaporation process is the flow of the molten aluminum from the center of the crucible to the opposing edges. This results in the need to continuously increase the output voltage of the transformer in order to maintain a constant current and therefore a constant deposition rate in order to ensure film quality and uniformity. The aluminum thickness was measured with a monitor wafer using profilometry. This thickness was consistently on the order of 200 nm, taking into account nonuniformities during the evaporation process.

Following deposition of the aluminum hard mask, the first lithography step is used to transfer the cantilever pattern onto the hard mask. The configuration after the first lithography step is shown in the quarter-dye illustration below in Figure 3.12.

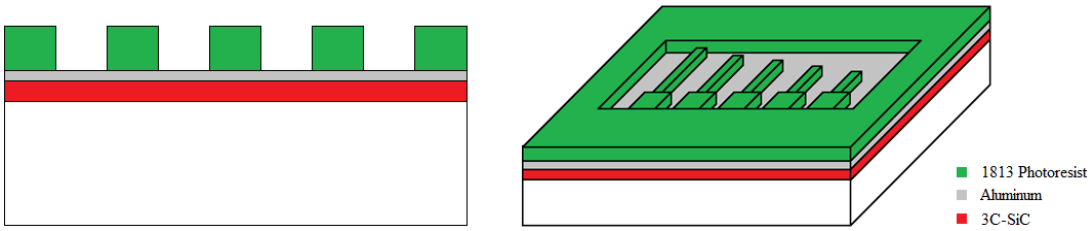

Figure 3.12: Quarter-dye schematic after 1st lithography step

The next step in the process involves a chemical wet etching of the exposed aluminum for which the 1813 photoresist acts as a mask. The chemical is a pre-mixed Transene – Type A solution which is heated to a temperature of 40 °C to achieve an approximate etch rate of 80 Å/second. In order to ensure a complete etch, the standard time for an aluminum thickness of 200 nm is three minutes which includes a 50% overetch. Immediately after etching the wafers are thoroughly rinsed, placed in a spin dryer, and optically inspected to ensure the quality of the etching process. The quarter-die view of the cantilevers at this point in the process is shown below in Figure 3.13.

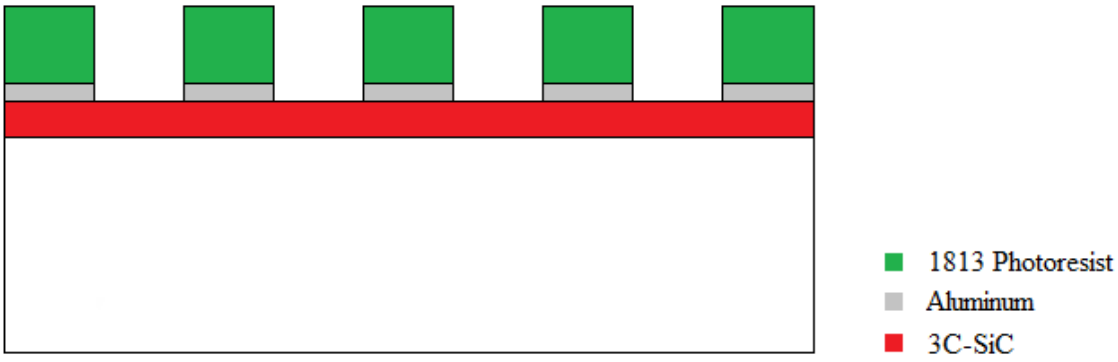

Figure 3.13: Quarter-die cross-section of process flow after aluminum etch.

The next part of the process involves plasma etching through the exposed 3C SiC down to the silicon substrate. For this part of the fabrication process an inductively-coupled plasma system was used to anisotropically etch the SiC. The ICP system used was the Alcatel AMS-100 deep reactive-ion etcher. A schematic of this system is shown below in Figure 3.14. The process parameters used to etch the 3C SiC films are shown below in Table 3.2.

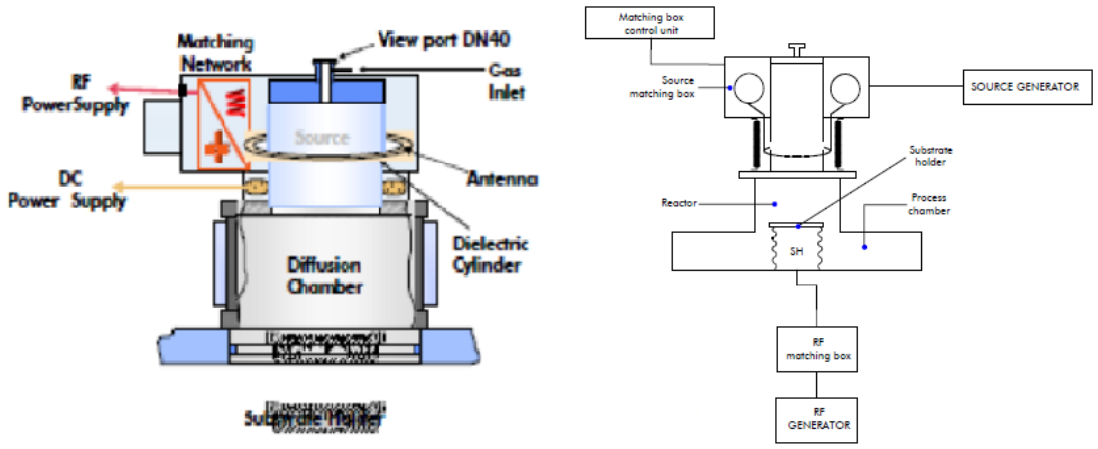

Figure 3.14: Illustration of Alcatel AMS-100 DRIE used in microcantilever fabrication.

Table 3.2: Plasma process used in DRIE etching of 3C SiC films.

Etching Process Parameter	***Nominal Value***
Pressure (mTorr)	4.125-4.725
SF_6 Flow (sccm)	80
O_2 Flow (sccm)	20
Applied RF Source Power (W)	1500
Applied RF Substrate Power (W)	80
Resulting V_{dc} bias (V)	~19
Helium Cooling Pressure (Torr)/Flow (sccm)	7.5/0.1

The next steps of the process flow involved the removal of the aluminum hard mask and the deposition of thin nitride and polysilicon films in order to perform the 2nd level lithography. The 2nd level lithography was necessary to isolate adjacent areas of each die in order to perform pre- and post-irradiation analysis. The Si_3N_4 film is ultimately used as a perfectly selective mask for the final KOH silicon etch and was deposited with a standard LPCVD process using ammonia (NH_3) and DCS (SiH_2Cl_2) as feed gases at a constant temperature of 775 °C.

Following the nitride deposition, a thin (~150 nm) polysilicon film was deposited in order to serve the dual purpose of providing the pattern transfer layer for the 2nd layer lithography and as an etch mask for the chemical etching of the Si_3N_4. The polysilicon deposition uses disilane (Si_2H_6) as the feed gas at a setpoint temperature of 630°C. The quarter-dye view of the cantilever process flow at this point is shown below in Figure 3.15.

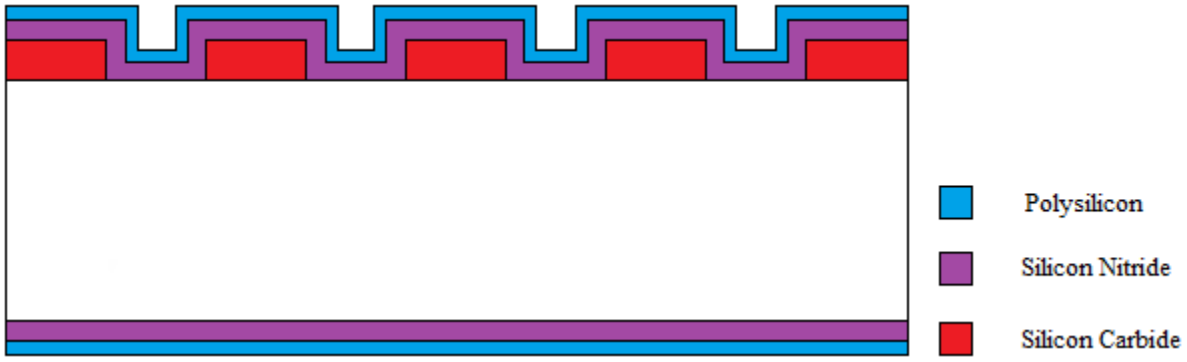

Figure 3.15: Quarter-dye cross sectional view of the process flow following silicon nitride & polysilicon deposition.

As is evident in Figure 3.15, the deposition of the silicon nitride and polysilicon was conformal with respect to the features. This was necessary in order to account for lateral etching of both films. At this point in the process flow, the 2nd level lithography mentioned previously is performed. The photolithography mask used for this is shown below in Figure 3.16.

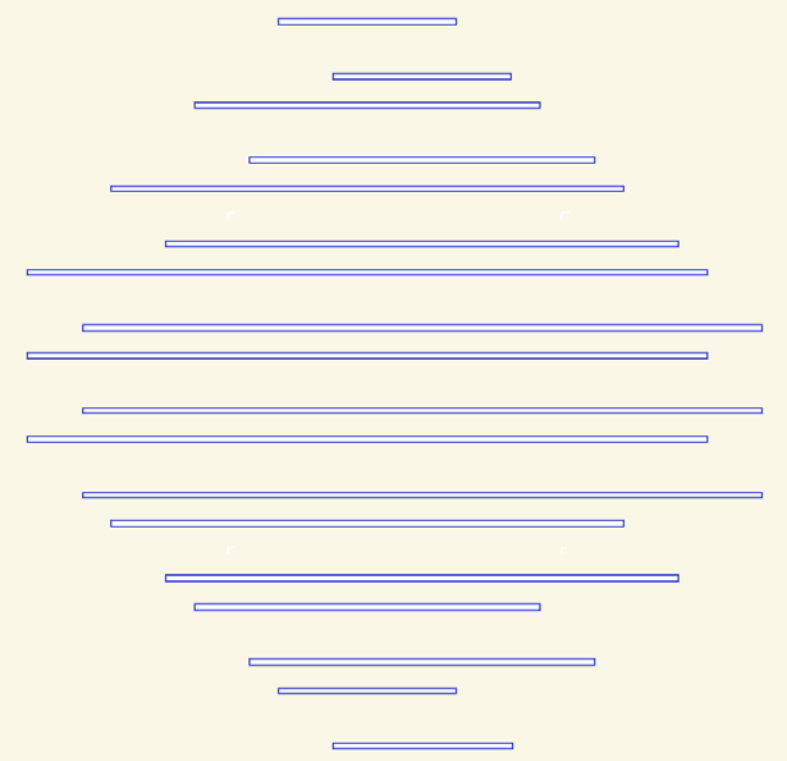

Figure 3.16: Second-level photolithography mask used in order to isolate adjacent sets of cantilevers on each die.

The 2nd-level lithography step forms a trench which is later transferred into the polysilicon layer by plasma etching. The quarter-die of the process flow after the final deposition step is shown below in Figure 3.17.

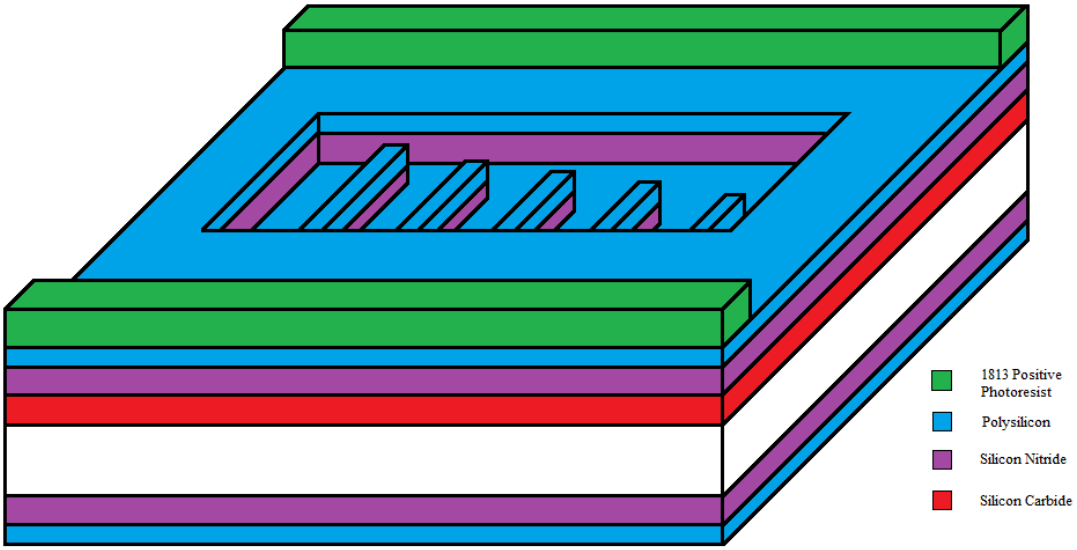

Figure 3.17: Quarter-die view of cantilevers following 2nd level photolithography.

The next step involves etching the trench pattern into the polysilicon film using the photoresist as the etch mask. The reactive-ion etch of the polysilicon was conducted in a CCP plasma system as discussed above. The plasma etching system used to etch the polysilicon was the Semigroup RIE 1000 TP. The process parameters used in the anisotropic polysilicon etch is shown below in Table 3.3.

Table 3.3: Plasma process used to etch polysilicon in KOH-based design process.

Etching Process Parameter	***Nominal Value***
Pressure (mTorr)	30
SF_6 Flow (sccm)	15
O_2 Flow (sccm)	7.5
Applied RF Power (W)	80
Resulting V_{dc} bias (V)	~ 132

By plasma etching the polysilicon, the material will only be removed from the top of the wafer unlike chemical etching which would remove polysilicon from the top and bottom of the wafer. This is important because the polysilicon film serves as the etch mask for the subsequent silicon nitride chemical etch and by only removing it from exposed areas on the top of the wafer, the polysilicon on the bottom of the wafer will prevent backside etching of the underlying silicon nitride. With the polysilicon being removed only from the trenches, the remaining photoresist is stripped from the wafer using a solution bath known as Nano-Strip™ which is roughly 90% sulfuric acid. Following the removal of the photoresist, the wafers are rinsed and placed in a spin dryer. The quarter-die progression of the process after the polysilicon plasma etch is shown below in Figure 3.18.

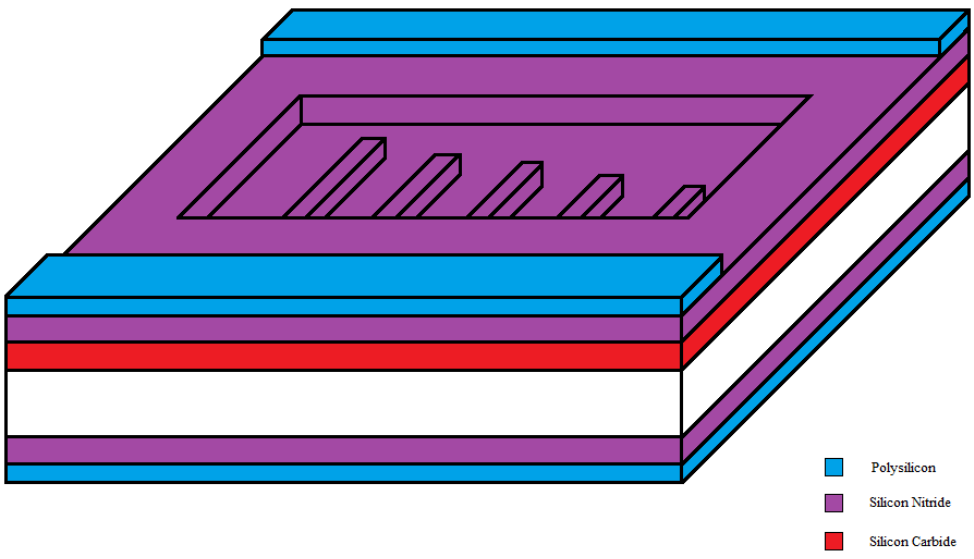

Figure 3.18: Quarter-die representation of the process flow following the plasma etching of polysilicon.

Following the polysilicon etching, the Si_3N_4 film is exposed only in the trenches where the cantilevers are released for pre-irradiation analysis. The next step of the fabrication process involves a hot phosphoric acid chemical etch in order to remove the silicon nitride to expose the silicon substrate. Only the silicon nitride not masked by the polysilicon will be etched in the hot phosphoric acid solution heated to 180 °C. The solution is pre-mixed and produced by Transene. The predicted etch rate was 12.5 nm/min and with an added overetch, the overall time of the silicon nitride chemical etch for an approximate thickness of 200 nm was 30 minutes. The progression of the wafer can be seen below in Figure 3.19 in the quarter-die illustration.

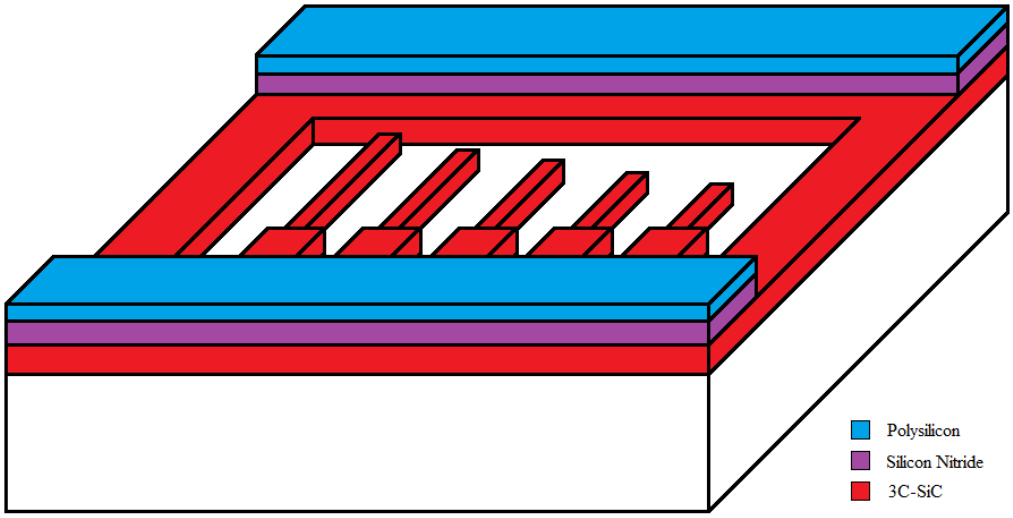

Figure 3.19: Quarter-die view following the silicon nitride etch

At this point in the fabrication process, the cantilevers are ready to be released using KOH chemical etching. It is important to mention that in order to use a specific wafer holder

for the KOH etch, which protects the sides from etching, it was necessary to use 300 µm thick silicon wafers. The cantilevers adjacent to the one shown in Figure 3.19 above remain covered by the polysilicon and silicon nitride and therefore remain unreleased. The KOH solution was heated to 80 °C and consisted of a KOH/deionized water ratio of 40%. The characteristic etching of KOH for (100) silicon occurs along the (110) planes as shown below in Figure 3.20.

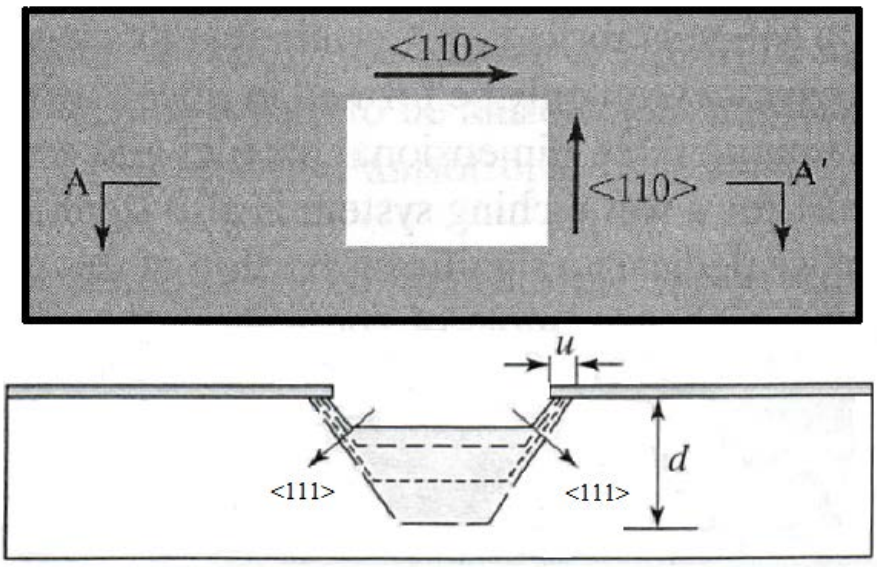

Figure 3.20: Progression of KOH chemical etch of (100) silicon. [LIU2]

For chemical etching of (100) silicon, the etch proceeds most quickly along the <100> and <110> directions, with the <110> coming out of the page when referring to Figure 3.20 above. Etching also occurs in the <111> direction but at a much slower rate than the others mentioned, however it is the etch rate in the <111> which ultimately allows for the termination of the etch at a point resulting in an inverse pyramidal structure. [LIU2] Based

on the size of the initial opening in the mask, the termination of the etch can be directly controlled.

The opening of the mask shown in Figure 3.20 was designed for a etch depth of 200 µm with the size of the opening being 583.2 µm. This opening was determined based on the longest cantilever beam (250 µm) plus the length of the anchor (50 µm). This mask design introduced the inaccuracy of releasing the entire anchor of the cantilever beam which dampens the true deflection of the cantilever beam based on the size of the anchor. The original mask design is shown below in Figure 3.21,

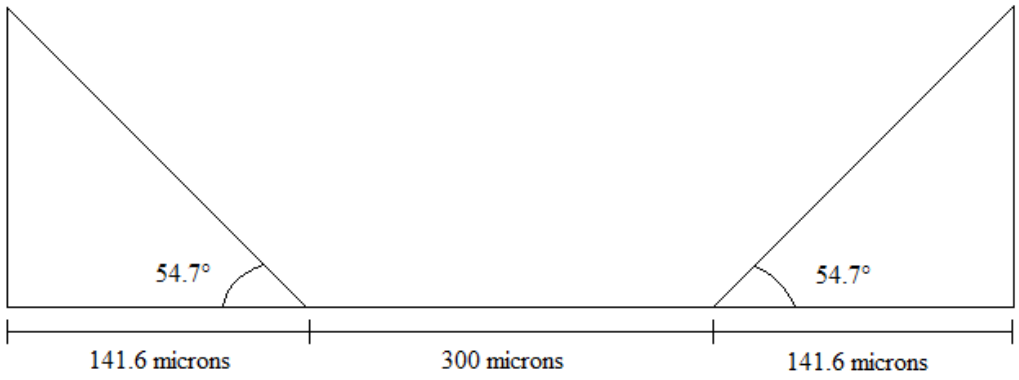

Figure 3.21: Original dimensions used to determine mask design for 1st level lithography

In order to correct this oversight, the open area of the mask shown in Figure 3.21 can be reduced by a total of 50 microns in order for the release point to occur at a point half the length of the anchor. Due to the cost and time constraints of making a new mask, a plasma-based work around was developed by using a low-bias, high pressure plasma etch which isotropically etched the silicon substrate underneath the thin-film SiC, while incurring

negligible lateral etching of the SiC cantilever beams. This etch was done using the previously mentioned DRIE system for which the process is shown below in Table 3.4.

Table 3.4: DRIE process parameters used in isotropic etching of silicon substrate in alternate design process flow.

Etching Process Parameter	***Nominal Value***
Pressure (mTorr)	5.6-5.85
SF_6 Flow (sccm)	80
O_2 Flow (sccm)	20
Applied RF Source Power (W)	1500
Applied RF Substrate Power (W)	9
Resulting DC Bias Voltage (V)	12-12.5
Helium Cooling Pressure (Torr)/Flow (sccm)	7.5/0.1

By using an isotropic plasma etch, the release point can be controlled by the duration of the etch. Based on initial characterization of the lateral etch rate of the process, the optimal time was determined to be 18.664 minutes. One issue with the initial characterization of the silicon etching process was filaments of silicon adhering to the SiC cantilever beams after release. This can be seen below in Figure 3.22 and was corrected by closing the throttle valve between the plasma chamber and the turbomolecular pump to the point where it was only 25% open. This increased the pressure in the chamber to value given in Table 3.4 above and reduced the mean-free path of the ions. Reducing the mean-free path of the molecular species in the chamber results in an increase in the local density of chemically reactive species and thus improves the isotropic etch characteristics.

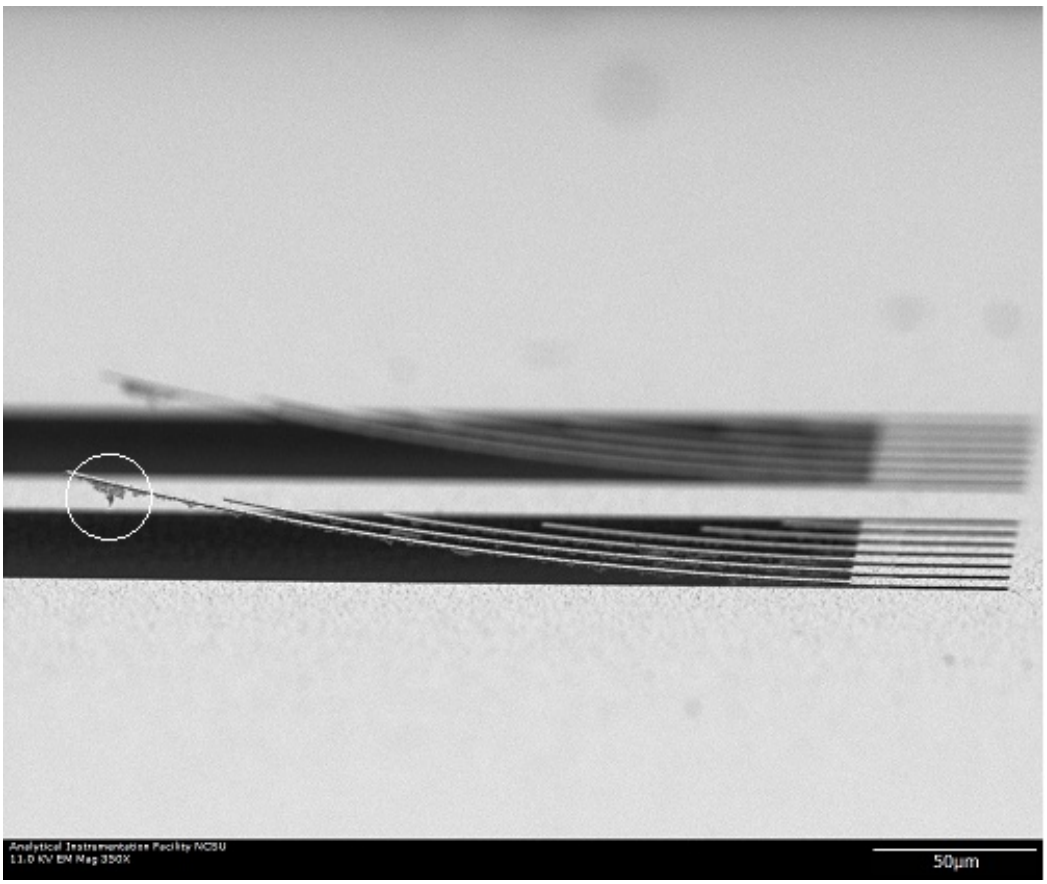

Figure 3.22: SEM image showing silicon attached to the SiC cantilevers after releasing from the bulk silicon substrate

The difference in the method of silicon etching on the release endpoint of the cantilevers is shown in the representative SEM images below in Figure 3.23.

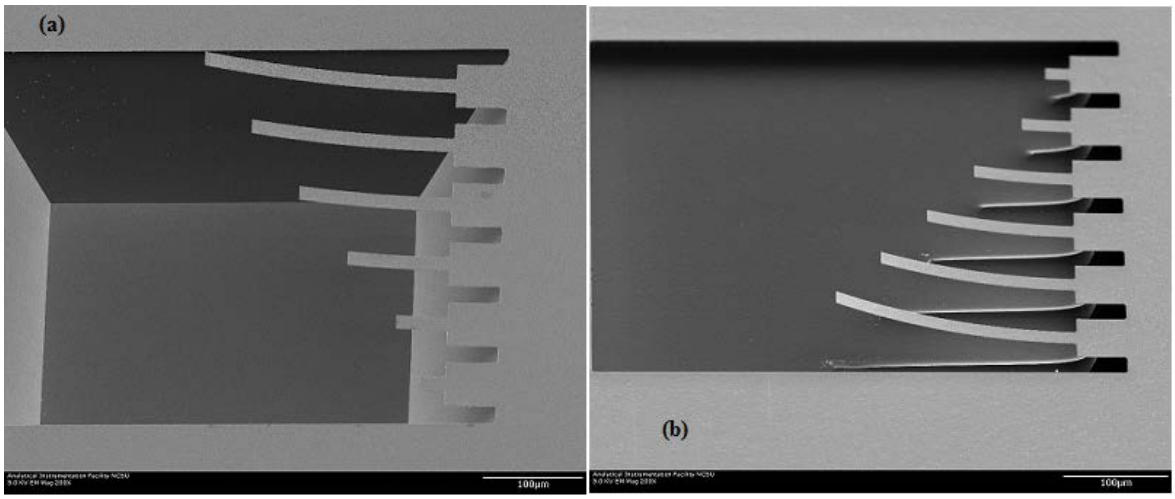

Figure 3.23: SEM Images of (a) cantilevers released using KOH and (b) cantilevers released by DRIE plasma etching.

These are images from wafers with (a) -201.333 MPa and (b) -159.333 MPa residual stress values. From Figure 3.23 (a) it is can be seen that with the photolithography mask as is, the release endpoint of the cantilevers extends through the full length of the anchor such that the entire anchor is entirely released and therefore contributes to the overall deflection of the beam. However, with the plasma-based process the release endpoint is directly controllable and is dependent on the duration of the etch alone. In Figure 3.23 (b) the ridges of silicon directly beneath the cantilever beams are a result of mutual repulsion of the fluorine ions and the non-zero RF current applied to the substrate holder of the DRIE system. The lateral endpoint of the isotropic silicon etch can be observed in greater detail in the SEM image shown below in Figure 3.24.

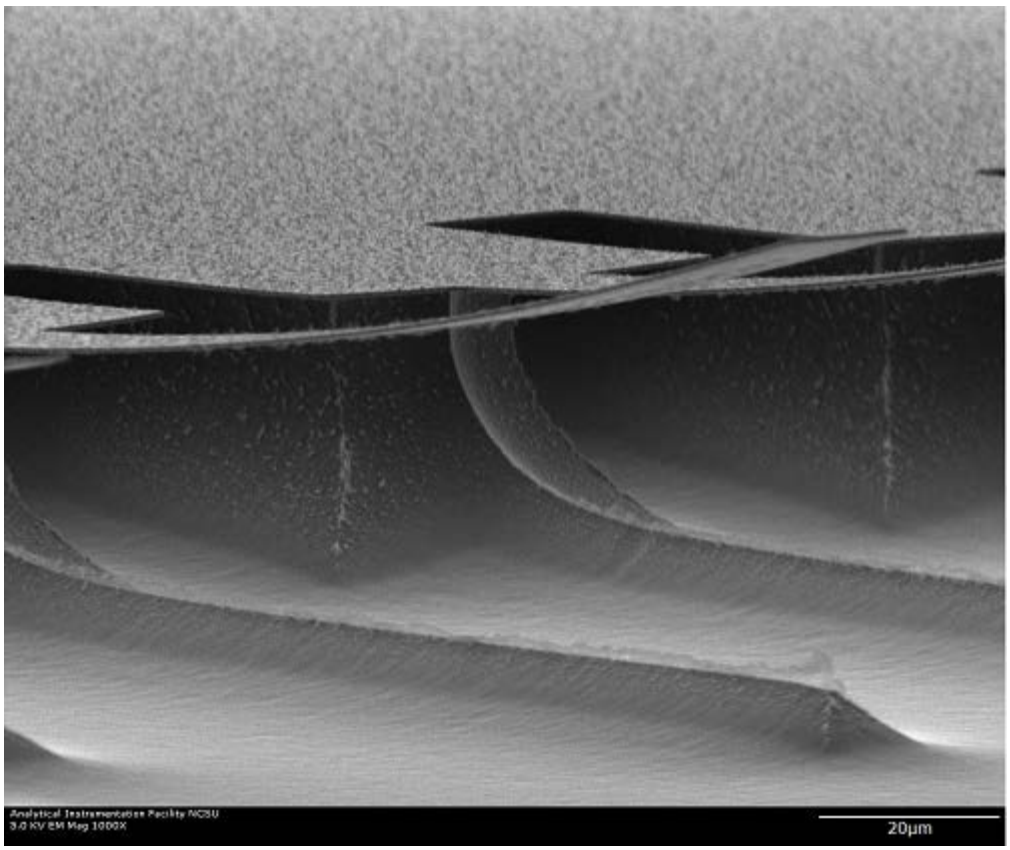

Figure 3.24: High magnification image of release point of microcantilevers using plasma-based fabrication process.

The additional need for a plasma-based cantilever release method was due in combination to the high residual stresses of the thin-film SiC and the evolution of crystalline changes as a result of radiation damage since the peak damage of all radiation experiments described later occurred in the silicon substrate. The change in the crystal structure of the silicon substrate is evident by the evolution of the (311) silicon peak in Figure 3.25 shown below.

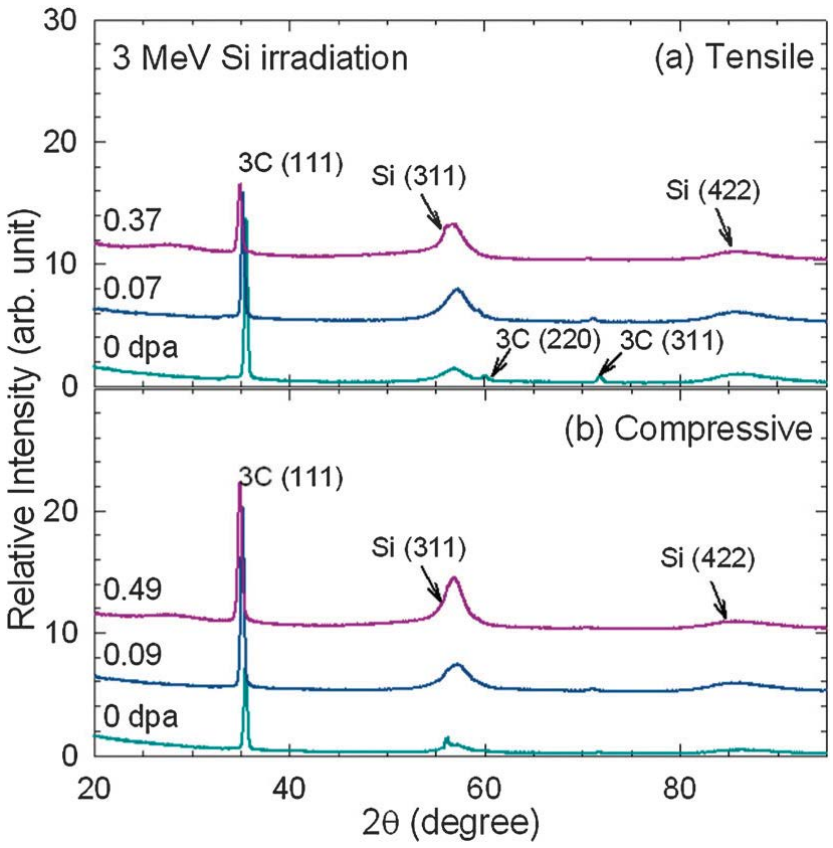

Figure 3.25: Evolution of prominent 3C SiC peaks after irradiation [ZHA2]

The evolution of the (311) Si peak and to a lesser degree the (422) Si peak as a result of increasing radiation dose is due to the amorphization of the Si substrate which changes the anisotropic KOH etching to the point that the stress effects at the edges of the features become problematic and the cantilever devices are destroyed. The destruction of the microcantilever devices as a result of the change in etching characteristics of the KOH chemical etch is shown below in Figure 3.26.

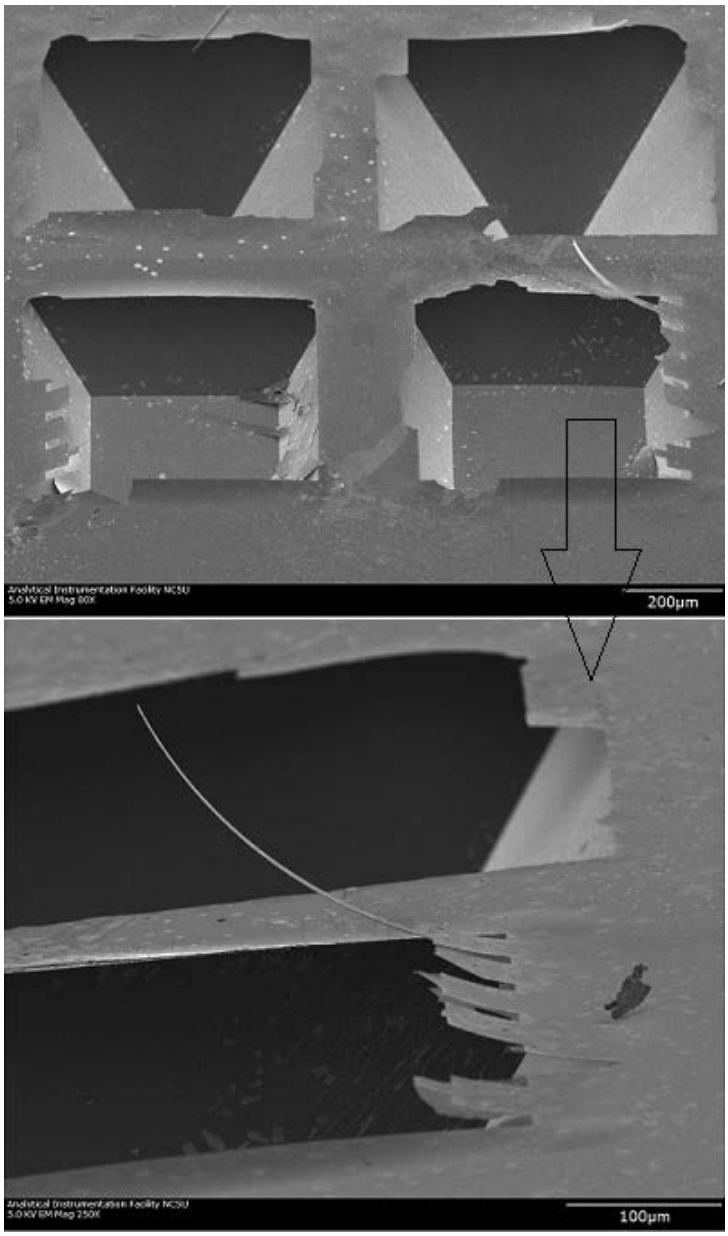

Figure 3.26: Stress-induced delamination due to altered KOH etch characteristics as a result of c-a transition of silicon substrate post-irradiation.

It was for this reason that an approach utilizing high density plasma etching was used both to etch the cantilever pattern into the SiC and to subsequently release the cantilevers from the silicon substrate.

The plasma-based process utilizes sputtered titanium and aluminum to act as hard masks for the etching process, since the polysilicon and silicon nitride used in the KOH process do not yield the selectivity necessary to conduct the plasma etching. As a result, ion irradiation needs to be done through the thin titanium hard mask in order to do post irradiation release. The first step in this process flow involves the DC sputtering of a 200 nm titanium film on the 3C SiC thin-film followed by the identical 1st level lithography as shown in Figure 3.27 below.

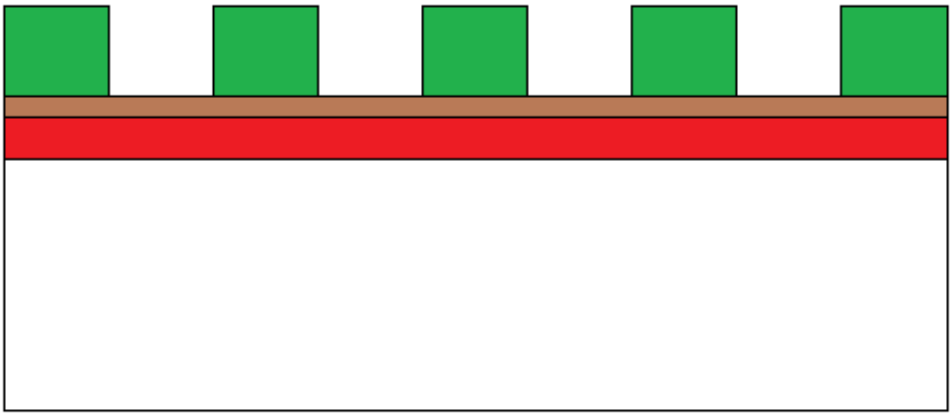

Figure 3.27: 1st level lithography for plasma-based process flow.

The titanium is then etched using a buffered oxide etch (BOE) solution which is essentially diluted hydrofluoric acid. The cross sectional view of the microcantilever following the titanium chemical etching is shown below in Figure 3.28 below.

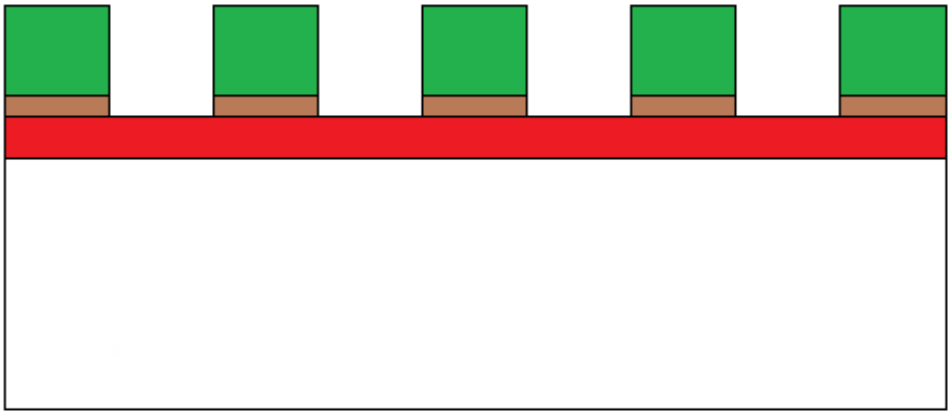

Figure 3.28: View of microcantilever following chemical etching of the titanium layer.

This now provides the cantilever pattern that can be etched into the SiC film. The next step in the process flow involves the DRIE plasma etching of the exposed SiC using the process described in Table 3.3. Following this etch, the deposition of a thin, 100 nm aluminum layer is conducted to serve as a sacrificial layer to do the 2nd level lithography which involves isolating two adjacent sets of cantilevers in each die. After deposition of the aluminum film, the 2nd level photolithography is performed and the exposed aluminum is chemically etched using the same solution as described in the KOH-based process flow the process progression is represented below in Figure 3.29.

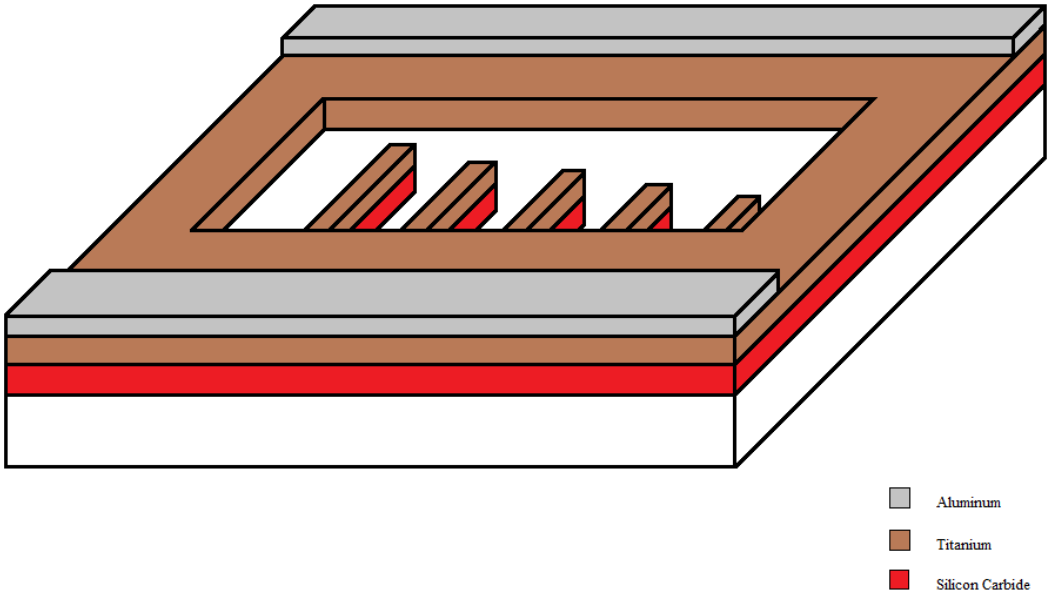

Figure 3.29: Progression following 2nd level photolithography and aluminum chemical etching.

The next step in the process flow involves the DRIE isotropic etch of the exposed silicon substrate in order to release the cantilevers. This process is shown above in Table 3.4 and has a high selectivity with respect to both the aluminum and titanium hard masks. Following this, the remaining exposed titanium is removed by BOE and the remaining aluminum is stripped by chemical etching and since the Transene solution described previously is selective with respect to titanium, the unetched titanium hard mask will not be removed. This process flow is still a work in progress due to the need to perform an additional 2nd level photolithography step after irradiation of the die.

CHAPTER 4: Analysis of Radiation-Induced Damage & Microstructural Effects

4.1 Radiation Damage in SiC

Investigating the applicability of SiC as a material for use in high-radiation environments requires understanding the effects of the damage formation and defect accumulation due to ion and neutron irradiation [GAO]. An example of the application of SiC in such environments is as a structural layer in fuel coatings for next-generation nuclear reactors such as the TRISO fuel design previously discussed. For use as a structural layer, it is important to consider how the film stress changes due to microstructural changes in the lattice structure as a result of defect production due to ionizing radiation. This is due to the fact that at radiation temperatures less than approximately 423 K, accumulation of strain due to defect production can exceed a critical level where amorphization occurs.[SNE] The low temperature amorphization implies that the most dramatic microstructural changes occur during radiation exposure at low temperatures. [SNE] The microstructural effects of both neutron and ion irradiation of 3C SiC indicates the formation of small clusters of self-interstitial atoms or dislocation loops which even at temperatures below several hundred Kelvin can lead to an accumulation of film strain which can directly lead to crystalline-to-amorphous transition (c-a transition).[SNE] This film strain is a result of the swelling effect observed in the SiC crystal structure. The figure shown below summarizes some of the experimental work and mechanisms associated with microstructural development of 3C SiC for a wide range of irradiation temperatures and fluences.[SNE]

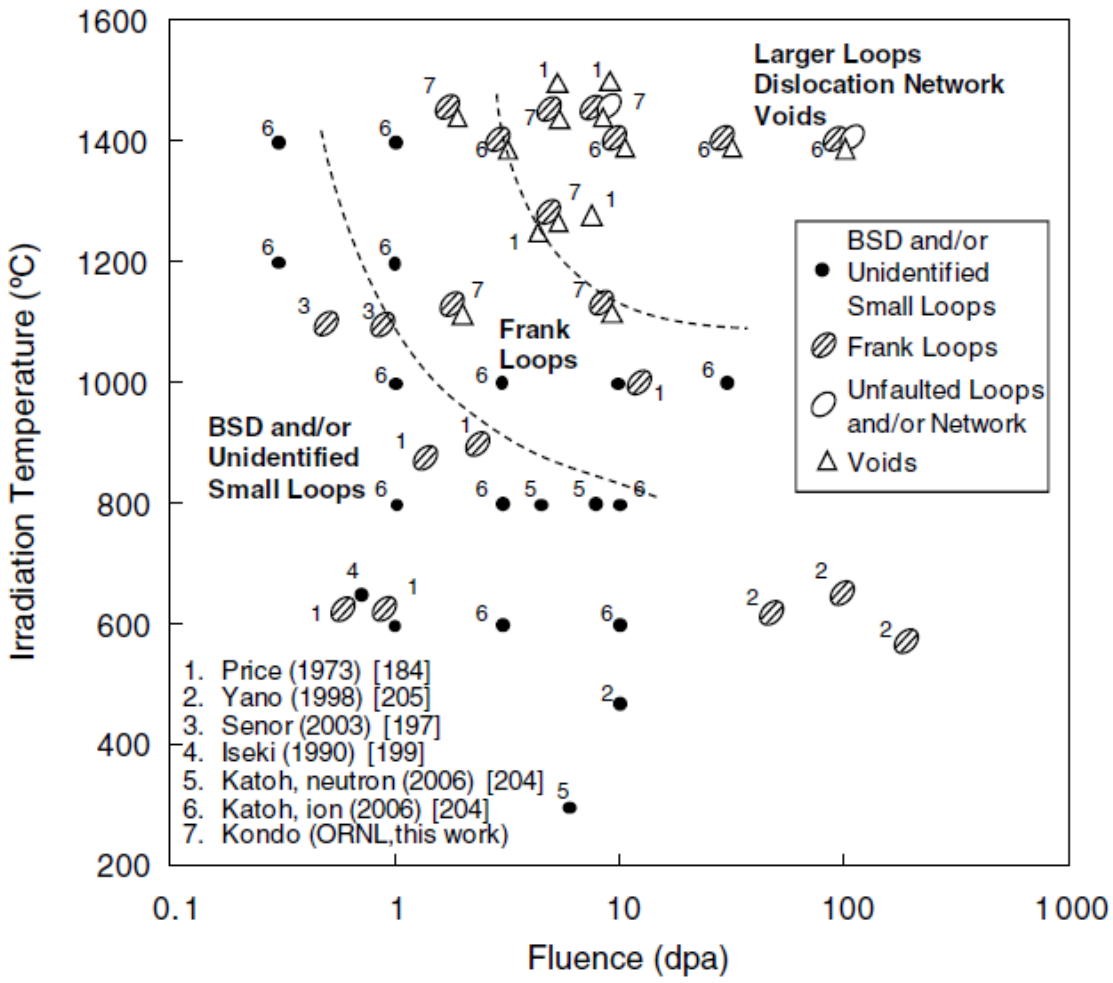

Figure 4.1 - Microstructural effects of neutron and self-ion irradiation temperature & dose for 3C SiC. [SNE]

From Figure 4.1 above it can be seen that for fluences below approximately 0.5 dpa, no defect clustering or networks is observed, although at fluences of 1 dpa and above dislocation loops and clusters, as well as voids have been observed.[SNE]

This swelling of the lattice structure as a result of microstructural defect clustering is an important characteristic in the applicability of SiC as a structural material. The

crystalline-to-amorphous (c-a) transition of SiC as a result of the ionizing radiation damage is an important aspect to consider for application of SiC in harsh environment MEMS and microelectronics. Both the increase in volume due to swelling and c-a transition changes both the mechanical and electrical properties of the SiC. It has been reported, at temperatures above the critical amorphization temperature the swelling increases logarithmically with dose until it reaches a saturation level. [SNE] Some insight into the change in the stress-strain characteristics due to defect related lattice damage can be determined by measuring adjacent microcantilever deflections pre- and post-irradiation in order to estimate the stress-strain gradient of the different residual film stress states.

The actual microstructure damage mechanisms are explained in terms of the Kinchin-Pease (K-P) model which is based on the minimum threshold displacement energy for the specific material. The minimum threshold displacement energy is the minimum kinetic energy that an atom in a solid material needs to be permanently displaced from its corresponding lattice site. For 3C SiC these displacement energies are assumed to be 20 and 35 eV for the C and Si sublattices, respectively. [ZHA2] In order for a permanent defect to be produced the kinetic energy received by the lattice atom from the incoming irradiation particle must exceed the required formation energy of a Frenkel pair (vacancy and knock-off lattice atom interstitial). Defect production resulting from ion irradiation depends on a number of variables including ion mass, energy, fluence and the temperature of film during irradiation. [ZHA2]

It has been shown that nanocrystalline SiC exhibits enhanced radiation damage tolerance due to the high density of grain boundaries where interstitial and vacancy

annihilation occurs. [ZHA2] However, the data regarding the influence of grain boundaries on defect production rates in nanocrystalline SiC varies widely from having a negligible effect on damage production to having a significant effect. [ZHA2] The presence of stacking faults, which are essentially self-layered interfaces, provide for significantly enhanced radiation tolerance. The experimentally grown 3C SiC exhibits high stacking fault densities, which is believed to account for the superior radiation damage tolerance explained in section 4.3.

4.2 Experimental Irradiation Details

In nuclear environments energetic neutrons transfer kinetic energy to silicon and carbon atoms in the lattice producing energetic silicon and carbon recoils that are responsible for the damage observed in SiC. Due to the fact that neutron irradiation in the NCSU Pulstar nuclear reactor would take several months to achieve the doses needed (0.5 dpa and above), it was more practical to study the effect of self-ion irradiation of the nanocrystalline 3C SiC in an ion beam accelerator. Since silicon ions are more efficient than carbon in producing damage the irradiation experiments were conducted using high energy silicon ions.

The irradiation experiments were performed using ion-beam accelerator systems at both Pacific Northwest National Laboratory (PNNL) and the University of Tennessee-Knoxville. To correlate stress-strain response to microstructural changes due to radiation damage, samples from two wafers at highly tensile and compressive stress states were irradiated with 3 MeV Si^{+} ions up to doses of 5.5 x 10^{15} ions/cm^{2}. The full conditions of the irradiation experiments are shown below in Tables 4.1 and 4.2 and are indicative of future irradiation conditions for cantilevers prepared using the revised fabrication process. The

beam spot size was a 3 mm x 3 mm square that contained one set of four cantilevers two released and two unreleased. The position on the wafer from which the samples were selected was based on the row number and cantilever set number and were selected from five points across the wafer to give a suitable spatial representation and variance in the stress gradient. These positions were based practically on which sets of cantilevers could actually be viewed in SEM at the 45° electron beam angle to the wafer.

Table 4.1: Summary of irradiation conditions on tensile-stressed cantilever samples (average 101 MPa)

Sample	***Beam Current (nA)***	***Implantation Time***	**Estimated Ion Fluence (cm^{-2})**
1	152 – 161	17 m 22 s	5.66×10^{15}
2	161-165	16 m 52 s	5.69×10^{15}
3	165	16 m 52 s	5.76×10^{15}
4	165	16 m	5.52×10^{15}
5	168	16 m	5.58×10^{15}
6	168	15 m 43 s	5.5×10^{15}
7	168	15 m 43 s	5.5×10^{15}
8	168	15 m 43 s	5.5×10^{15}

Table 4.2: Summary of irradiation conditions on compressively-stressed cantilever samples (average -198.667 MPa)

Sample	***Beam Current (nA)***	***Implantation Time***	**Estimated Ion Fluence (cm^{-2})**
1	168	15 m 43 s	5.47×10^{15}
2	164	15 m 43 s	5.40×10^{15}
3	164	16 m 6 s	5.48×10^{15}
4	164	16 m 6 s	5.45×10^{15}
5	162	16 m 48 s	5.65×10^{15}
6	160	16 m 18 s	5.45×10^{15}
7	160	16 m 30 s	5.5×10^{15}
8	160	16 m 30 s	5.5×10^{15}

Prior to the irradiation experiments being performed, simulations were run using the Stopping Range of Ions in Matter (SRIM) Monte-Carlo package. Using this simulation software, the exact thickness of the two 3C SiC thin-films, and the incident ion energy, the Frenkel pair formation, peak damage location, and ultimately the dpa can be estimated. The cantilever device wafers that were irradiated under the conditions shown in Table 4.1 and 4.2 above, were simulated in SRIM in order to determine the proper ion energy and most importantly the location of the peak damage caused in the SiC-Si stack.

The SRIM simulations were performed for the device wafers with residual stresses indicated in Tables 4.1 & 4.2 and had average thicknesses of 425.24 nm and 625.06 nm, respectively. Shown below in Figures 4.2 & 4.3 are the simulation results of 3 MeV Si^{2+} ion bombardments depicting the peak damage location and the ion ranges, respectively.

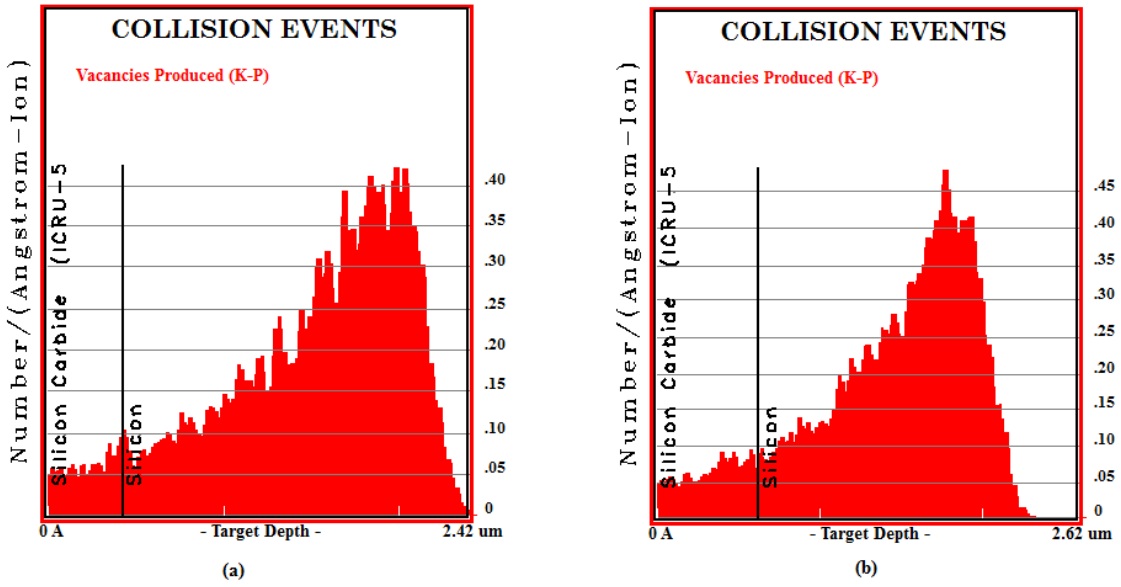

Figure 4.2: Peak damage profile of simulated cantilever device wafers (a) tensile stress state (b) compressive stress state using KOH-based process.

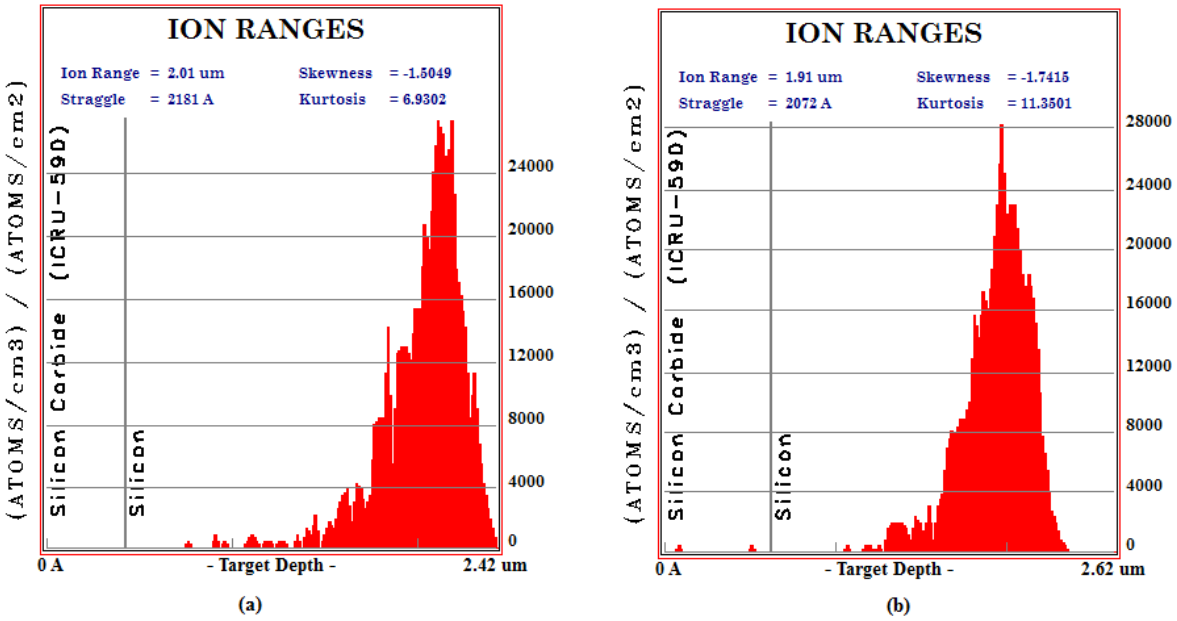

Figure 4.3: Estimated ion ranges for simulated device wafers in (a) tensile stress state (b) compressive stress state using KOH-based process.

For experiments to be performed on cantilever devices fabricated using the revised plasma-based process flow the ion bombardment would currently have to be performed through a thin titanium hard mask of approximately 200 nm. Therefore in order to predict the damage profile and ion range for future experiments, SRIM simulations for a stack consisting of 200 nm of titanium on 500 nm of 3C SiC on a silicon substrate were conducted and the results are shown below in Figure 4.4.

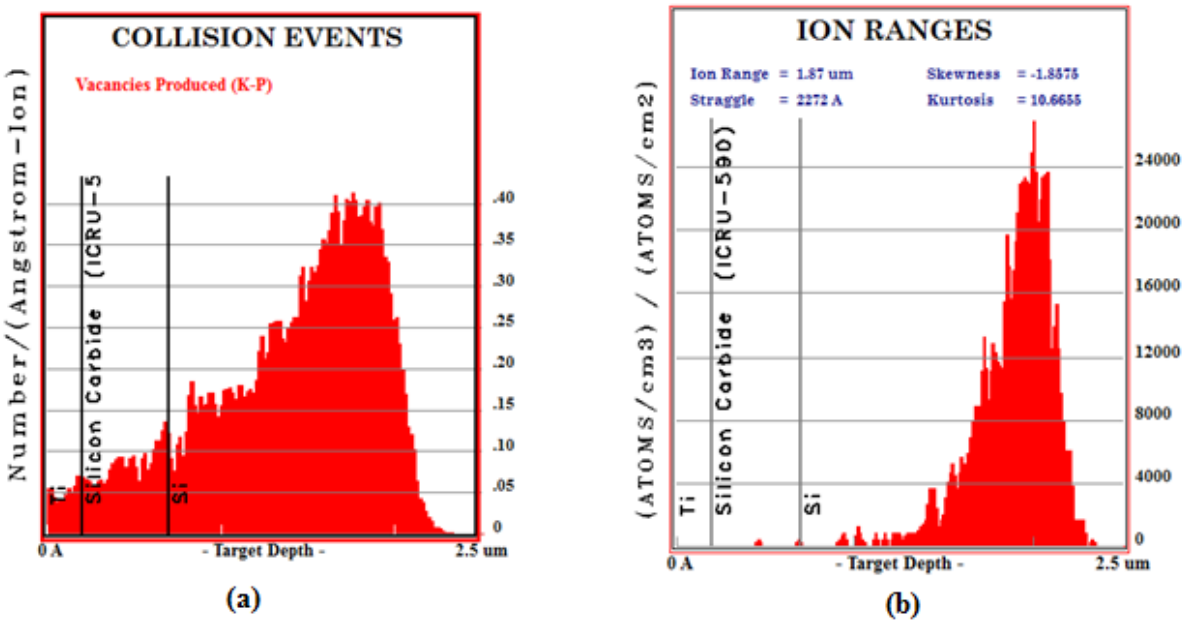

Figure 4.4: Damage profile (a) & ion range (b) for simulated configuration of cantilever samples prepared using the revised plasma-based process.

Comparing Figures 4.2 & 4.4 it is apparent that the peak damage in the SiC layer is approximately 0.14 compared to 0.1 for the samples that were fabricated using the KOH-based process. This increase in damage occurring in the SiC is due to the loss of kinetic energy of the ion as it passes through the titanium mask layer and would therefore yield a slightly higher dose for the same ion energy and fluence.

Additional experiments were performed by Zhang et al. on bare films of the experimentally grown polycrystalline 3C SiC to extrapolate the dose for c-a transition. For these experiments highly tensile and compressive films with average thicknesses of 445 and 750 nm, and average residual film stresses of 530 and -155 MPa, respectively were irradiated along the surface normal with 3 MeV Si^{+} ions with fluences up to 6.6 x 10^{15} cm^{-2}. An

additional experiment was performed on the tensile sample at an even higher fluence of $3x10^{16}$ cm^{-2} in order to better estimate the dose needed for full amorphization of the 3C SiC.

4.3 Radiation Tolerance in Engineered 3C SiC Films

It has been shown by colleagues at University of Tennessee-Knoxville that based on the inverse peak width of the characteristic (111) 3C SiC peak characterized using GIXRD such as that shown in Figure 3.6, the dose required for complete amorphization of the engineered, nanocrystalline 3C SiC occurred at around 3 dpa. This was based on GIXRD scans of several different tensile and compressive stressed samples and is shown below in Figure 4.5.

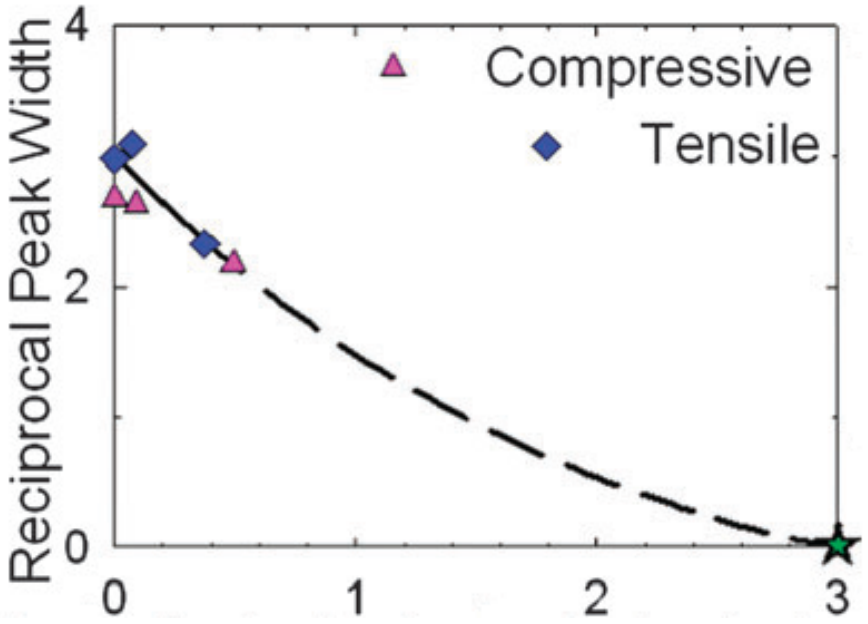

Figure 4.5: Extrapolation of the approximate dose required for complete amorphization of experimentally-grown 3C SiC. [ZHA2]

The units of the reciprocal peak width are degrees inverse and were determined based on the decrease in the full width half maximum (FWHM) of the characteristic (111) 3C SiC peak with increasing irradiation dose. The fit was based on the evolution of the peak width observed in the XRD analysis and correlated to the evolution of the microstructure in TEM using electron diffraction.

The sharp (111) 3C peaks shown in Figure 3.26 indicate that the crystalline structure of the 3C SiC film is well-retained up to doses of 0.49 dpa. Some broadening of the (111) peaks occurs at those higher doses up to 0.49 dpa which was attributed to some increasing amount of disorder due to the accumulation of point defects. [ZHA2] This GIXRD data correlates with TEM data which exhibits very little change in the layered SF structure and is shown below in Figure 4.6 for doses up to 0.49 dpa. [ZHA2]

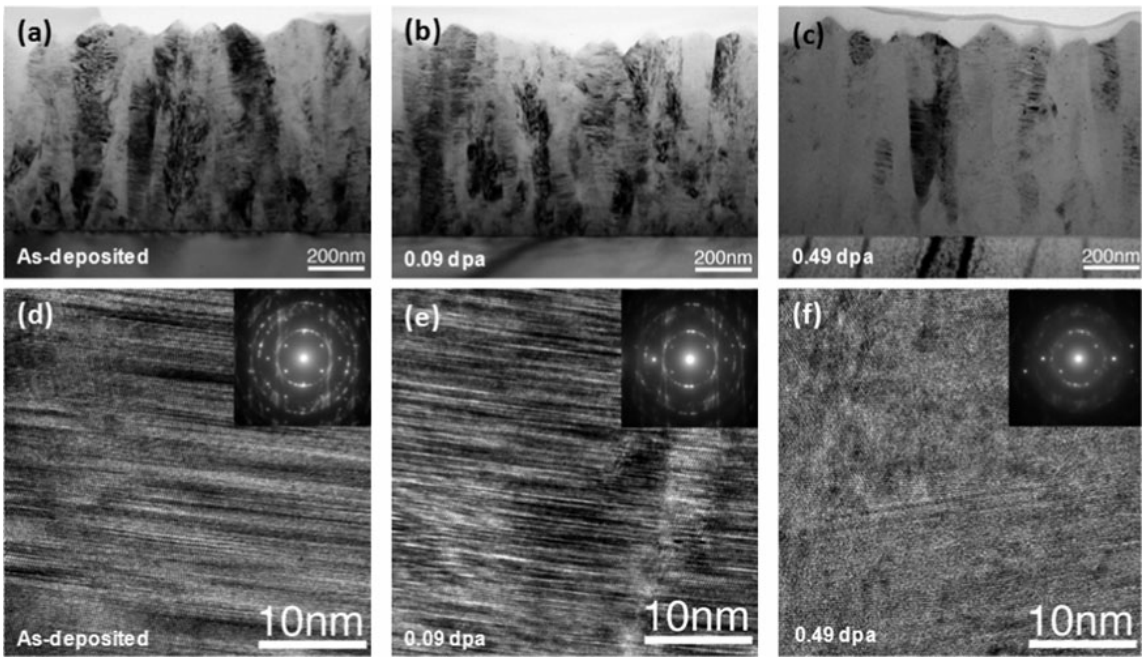

Figure 4.6: TEM Images of tensile films (a & d) as-deposited, (b & e) irradiated to 1.2 x 10^{15} cm^{-2}, 0.09 dpa, and (c & f) irradiated to 6.6 x 10^{15} cm^{-2}, 0.49 dpa. The electron diffraction patterns in (d), (e), and (f) show the evolution of the crystalline structure with increasing irradiation dose. [ZHA2]

It can be seen Figure 4.6 that the crystalline structure does not show a great deal of change up to a dose level of 0.49 dpa with is confirmed by GIXRD shown in Figure 3.6. At the highest dose it is apparent from (f) in Figure 4.6 that the film exhibits a certain degree of amorphization especially near the SiC/Si interface. Due to the nature of ion-solid interactions, non-uniform irradiation damage is produced along the ion path, with the dose level increasing to approximately 3.5 dpa near the interface. [ZHA2]

Overall the tolerance of the engineered nanocrystalline 3C SiC to radiation damage is greater than single-crystal 3C SiC. Zhang et al. report an order of magnitude difference in the radiation tolerance compared to that of single crystal 3C SiC. Approximately 80-85% of

point defects that would survive in single crystal 3C SiC may be annealed out in the experimentally-grown nanocrystalline 3C SiC. [ZHA2]

The decrease in the point defect survivability in the engineering 3C SiC may result from enhanced annihilation of the point defects at the nano-sized grain boundaries (GBs). It is well established that GBs act as sinks for defects of all types. Molecular dynamic simulations performed have shown that GBs, which are prevalent in nanomaterials, can capture interstitials and then release them back into the lattice to recombine with mobile vacancies that are within a few nanometers of the boundary. Because nanomaterials have a high proportion of boundary to bulk area, a majority of the vacancies introduced will be located within this short range of a GB. [ACK] It has been proposed that the contributions of GBs alone does not account for the enhanced radiation tolerance in the experimentally developed, nanocrystalline 3C SiC and that an additional source of defect annihilation is due to the high density of SFs within the individual grains. It has been proposed by Zhang et al. that the SFs promote point defect recombination and annihilation through less defect production, increased mobility of silicon interstitials, changes in defect survivability within or near the faults, and some degree of restriction of the normal random walk diffusion of interstitial defects. [ZHA2]

CHAPTER 5: Cantilever Deflection Results & Discussion

5.1: Pre-Irradiation Cantilever Deflection & Strain Gradient Analysis

In order to quantify the effect of microstructural damage as a result of the addition of defects and lattice disorder due to irradiation the methodology described above was developed in order to measure cantilever deflections of adjacent points on the wafer. Due to the sample preparation necessary for the ion irradiation experiments, the unirradiated cantilever deflection was measured prior to irradiation of the adjacent, unreleased set of cantilevers. As previously mentioned, due to a mask design error the KOH-based process was replaced with the plasma-based process to provide a more accurate representation of the pre-irradiated cantilever deflection.

In order to quantify the role of residual stress determined by profilometry and the Stoney relations on the stress variation through the thin-film thickness, a wide range of residual stress states were analyzed using the microcantilever deflections measured by SEM. These SEM measurements were made with the samples at a 45° angle relative to the electron beam, which required that a cosine error be figured in to the final corrected beam deflection shown in Eq.5 shown below:

$$Z_c = Z_m \cos(45°) \qquad \text{Eq.5}$$

where Z_C is the corrected deflection and Z_M is the initially measured deflection.
The strain gradient is then determined by Eq.11 discussed in Appendix A, which assumes that the strain gradient varies linearly with film thickness.

The residual stress states measured using the wafer curvature method ranged from -208.667 to 673 MPa. The averaged deflections of microcantilevers at various locations on each wafer were measured using SEM and the results are presented below in Figure 5.1 as strain gradient as a function of residual film stress.

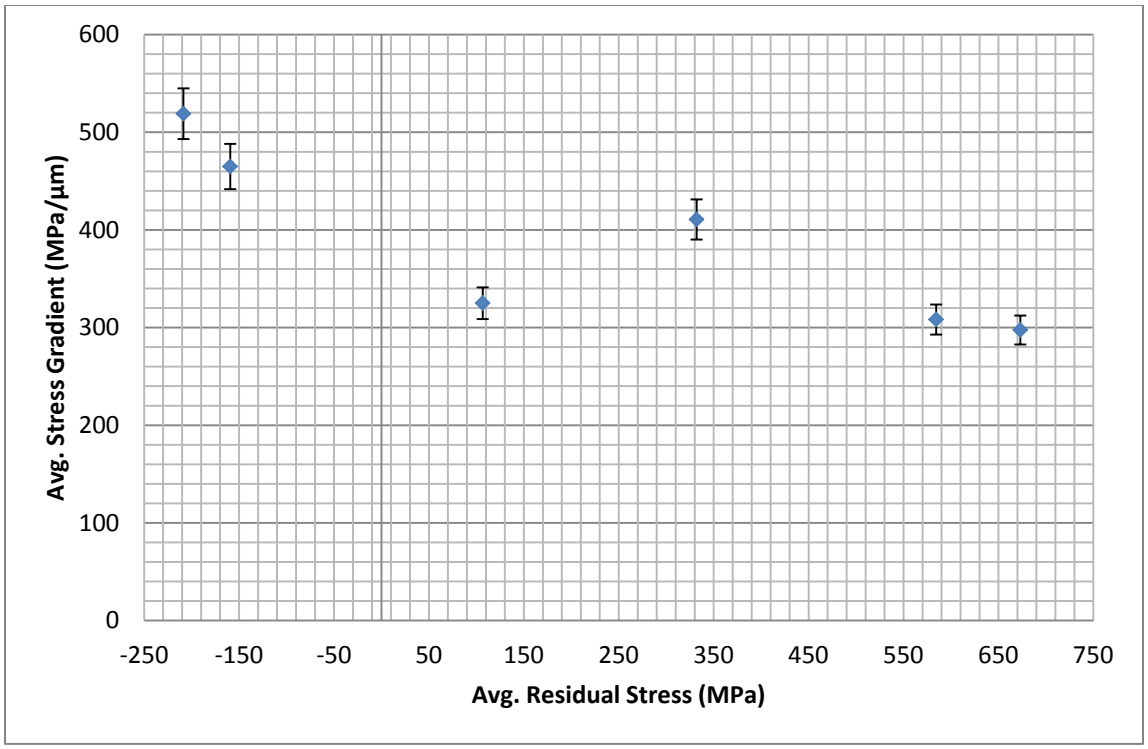

Figure 5.1: Relationship between the average stress gradient of 3C SiC films determined by measurement of cantilever beam deflection and average residual stress measured after growth process.

The analysis of the SEM images of the pre-irradiated released cantilevers involved measurement of the beam-tip deflection relative to the axis of the cantilever beam and the beam length not including the anchor since with the plasma-based process the anchor

remains attached to the silicon substrate. Sample measurements are shown below in Figure 5.2 for highly tensile and compressive stress states.

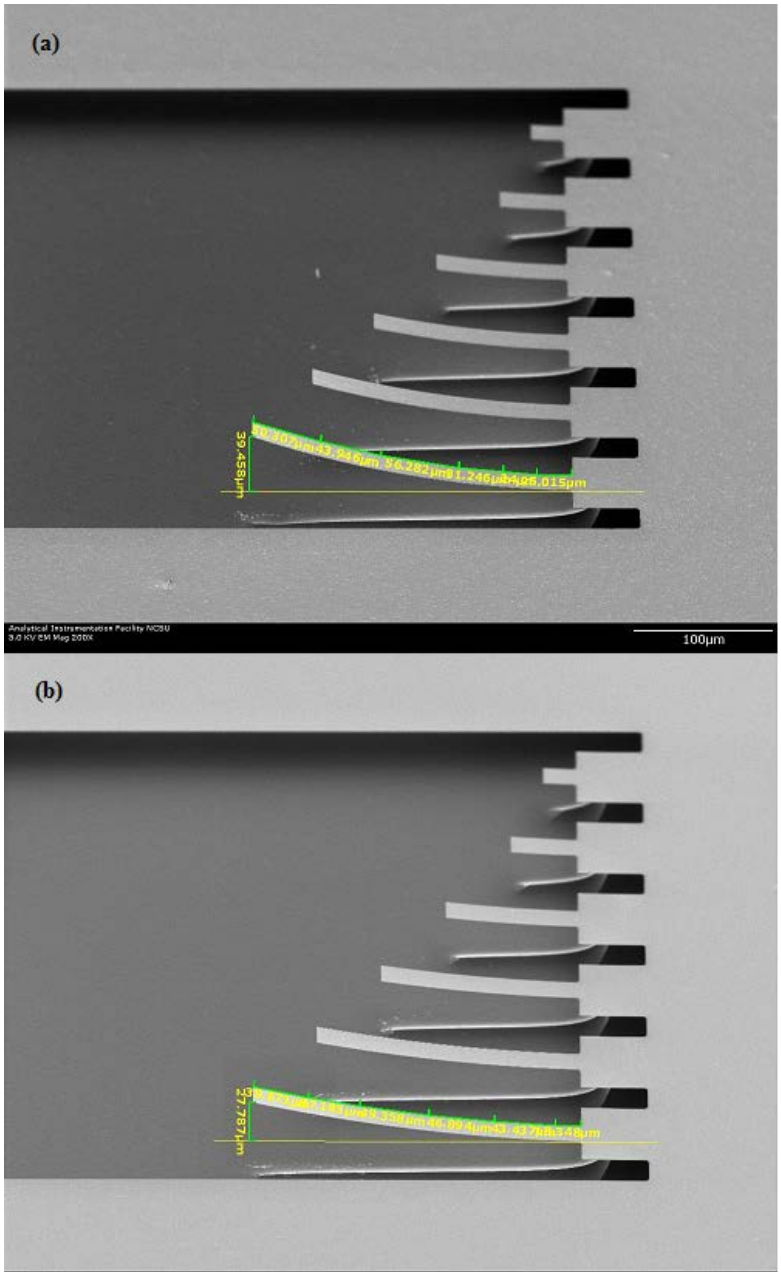

Figure 5.2: Sample SEM images & measurements of released cantilever sets for (a) highly compressive and (b) highly tensile stress states.

From Figure 5.2 it can be observed that for these example stress states, the sample with the compressive residual film stress has, in fact, a stress gradient which is more tensile near the surface of the thin film than the sample with a tensile residual film stress. This behavior is shown pictorially below in Figure 5.3.

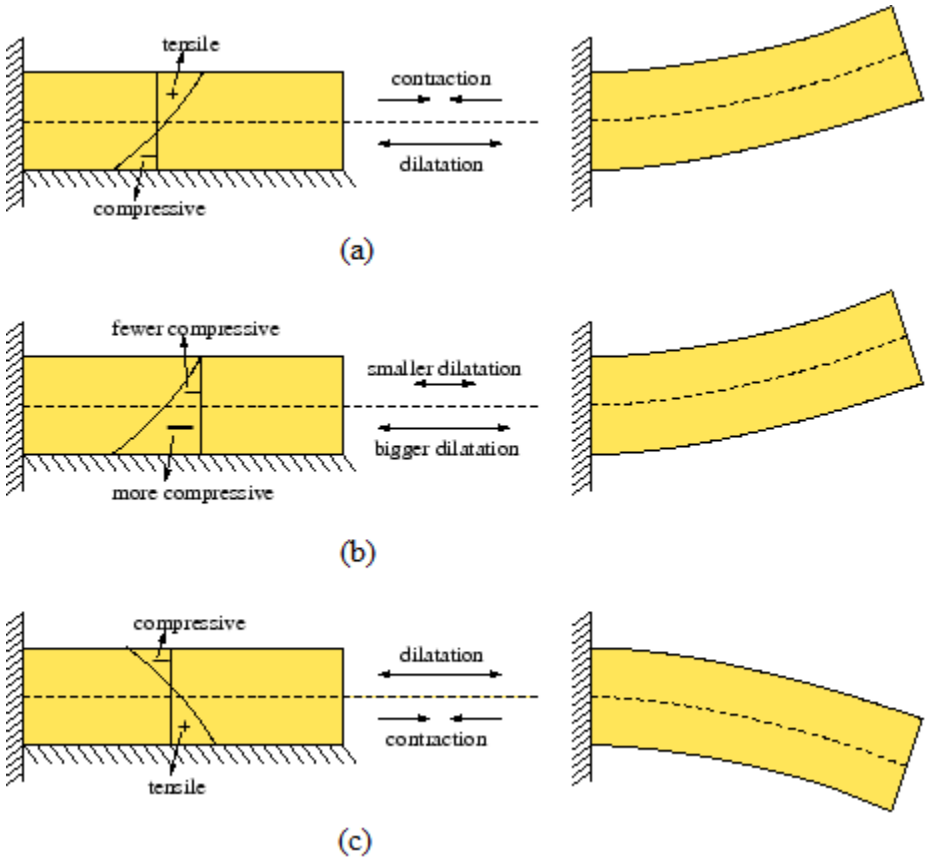

Figure 5.3: Illustration relating stress gradient over film thickness to cantilever deflection characteristics. [HOL]

In Figure 5.3 (a) the film has a positive stress gradient. The material above neutral axis is in a tensile state while the part below is in a compressive state. It is typical convention that

upon release the upper tensile part contracts and the compressive part expands such that the overall deflection is in the +z direction. Figure 5.3 (b) demonstrates that it is not necessary to have opposing stresses above and below the neutral axis of the cantilever beam. All stresses have a compressive character but due to the positive stress gradient the compressive stress and bending moment below the neutral axis are larger than that above ultimately resulting in a net upward deflection.

The variation in the cantilever deflection and length, with respect to wafer position, is shown for the deposition pressures depicted above in Figure 5.2 is shown below in Table 5.1.

Table 5.1: Variation in pre-irradiated microcantilever deflection & post-release length

Pressure (mT)	σ^2 ***in*** Z_C ***(μm)***	σ^2 ***in L (μm)***
210	0.22227	96.90881
274	1.54438	5.46332
325	0.29147	10.12560
380	0.05152	12.97380
451	0.03435	1.00826
464	0.29171	16.55049

From Table 5.1 the variance in the length of the released microcantilever beams is quite large in some of the samples analyzed with respect to the average released length. This is contrary to what was expected which is that the length change should be fairly consistent across the wafer with respect to the residual film stress of the film.

CHAPTER 6: Conclusions & Future Work

6.1 Conclusions

This project focused on developing a MEMS-based methodology to correlate the change in the stress characteristics of engineered nanocrystalline, 3C SiC thin films due to microstructural changes caused by radiation damage to the material. In order to characterize the effect of deposition pressure on the wafer-averaged residual film stress, the curvature of the silicon wafers were measured using profilometry before and after the growth of the thin 3C SiC films. It was first necessary to characterize the LPCVD process with changing pressure. From Figure 2.6 it is apparent that the deposition rate was relatively constant at low and high pressures with a linear increase as a function of pressure over the approximate pressure range from 300 to 400 mT. This linear increase in the growth rate coincided with a linear transition from tensile to compressive residual stress states which can be seen in Figure 3.3. This is attributed to the increase in nucleation sites and confined lateral grain growth owing to an increase in process pressure.

In order to quantify the stress characteristics on the same dimensional scale as the film, 1 cm x 1 cm dies with four sets of microcantilevers were fabricated and the deflection measured using SEM in order to correlate the deflection to the strain gradient over the thickness of the 3C SiC film. The process was designed such that adjacent sets were isolated from one other so that two sets could be released prior to irradiation and the other two post-irradiation. The pre-irradiation deflection results as a function of residual stress measured for the entire wafer is shown in Figure 5.1. From Figure 5.1 it is apparent that for films with a

more compressive residual stress state the strain gradient is larger and the deflection occurs in the positive z-direction. This was contrary to what was expected. It was predicted that a film with a compressive stress would deflect in the –z direction and tensile films would deflect in the +z direction. The observed deflection behavior is explained by the fact that the stress gradient of the compressive films is less compressive near the surface of the thin-film which results in a greater positive deflection than the films with high tensile residual stresses. In addition, it was hypothesized that upon release from the silicon substrate, the length of the cantilever beams would expand or shrink based on the residual stress of the thin-film. However, it can be seen in Table 5.1 that the variation in the length change is inconsistent with regards to residual film stress. It is unclear if the strain gradient in the compressive films is simply more compressive near the interface of the SiC and silicon as shown in Figure 5.3 (b) or if there is an actual transition from compression to tension as shown in Figure 5.3 (a).

Irradiation experiments were conducted using the ion beam accelerator systems at PNNL and UT-Knoxville with colleagues in order to determine the microstructural evolution. It was shown with GIXRD and high-resolution TEM that very little c-a transition occurs in the experimentally-grown 3C SiC thin films as can be seen in the very small broadening of the characteristic (111) 3C peak for 3C SiC films irradiated with silicon self-ion doses up to 0.49 dpa. Electron diffraction patterns confirm this showing very little change in the diffraction patterns of samples irradiated up to 0.49 dpa. Using this data it has been estimated that the dose required for c-a transition of the nanocrystalline 3C material is approximately 3 dpa. This has been estimated to be a full order of magnitude greater

radiation resistance over single crystal 3C SiC. It has been theorized that the enhanced radiation resistance is due to a combination of the well known effect of GBs acting as centers for recombination of point defects and the enhanced effect of SFs in providing a localized means of recombination owing to the restricted movement of point defects.

6.2 Future Work

Due to several time constraints a great deal more work is needed in investigating the behavior of the thin film stress characteristics as a result of radiation damage and the microstructural evolution. Firstly, due to the amorphization of the silicon substrate during irradiation of the original cantilever samples, additional irradiation experiments are needed for the plasma-based fabricated cantilever samples in order to finally quantify the change in deflection and therefore stress gradient as a result of microstructural damage of the 3C SiC films. In addition, a new device design layout is planned to improve the process of measuring the cantilever deflection pre- and post-irradiation.

In order to attempt to prove experimentally what has been shown using molecular dynamic (MD) simulations, that the high SF densities present in the nanocrystalline 3C SiC films enhance the radiation resistance of the 3C SiC, a new round of experiments has been planned to try and gain better control of the SF densities without changing the temperature of the LPCVD process. Based on review of existing literature, the first proposed experiments involve removing the carbonization step from the growth process and replacing it with an increased acetylene: DCS step as a way of controlling the crystallinity of the initial seed layer for subsequent film growth.

Finally, irradiation experiments performed on samples from the initial tests to attempt to control the SF densities need to be examined using high-resolution TEM mainly for conducting electron diffraction to determine the evolution of the diffraction pattern as an indication of the microstructural damage. In addition further analysis using XRD needs to be conducted in order to determine the change in crystal structure as a function of accumulated damage to the microstructure in order to determine the impact of SF density on observed damage levels.

REFERENCES

[ACK] Ackland, G. (2010). Controlling radiation damage. *Science (New York, N.Y.)*, *327*(5973), 1587–8. doi:10.1126/science.1188088

[ANZ] Anzalone, R., Locke, C., Carballo, J., Piluso, N., Severino, A., D'Arrigo, G., Volinsky, A.A., et al. (2010). Growth Rate Effect on 3C-SiC Film Residual Stress on (100) Si Substrates. *Materials Science Forum*, *645-648*, 143–146. doi:10.4028/www.scientific.net/MSF.645-648.143

[BAI] Bai, X.-M., Voter, A. F., Hoagland, R. G., Nastasi, M., & Uberuaga, B. P. (2010). Efficient annealing of radiation damage near grain boundaries via interstitial emission. *Science (New York, N.Y.)*, *327*(5973), 1631–4. doi:10.1126/science.1183723

[CAR] Carballo, J. (2010). Residual stress analysis in 3C-SiC thin films by substrate curvature method. Retrieved from http://scholarcommons.usf.edu/etd/1590/.

[CAP] Capozzoli, Peter M. (2006). Structural and Electrochemical Characterization of Two Proton Conducting Oxide Thin Films for a Microfabricated Solid Oxide Fuel Cell. Retrieved from http://dspace.mit.edu.

[CHA1] Chason, E., Sheldon, B., Freund, L., Floro, J., & Hearne, S. (2002). Origin of Compressive Residual Stress in Polycrystalline Thin Films. *Physical Review Letters*, *88*(15), 156103. doi:10.1103/PhysRevLett.88.156103

[CHE1] Cheung, R., Zorman, C., Fu, X., Mehregany, M., Pearton, S. J., Zappe, S. (2006). *Silicon Carbide Micro Electromechanical Systems*. (R. Cheung, Ed.) (pp. 1–15, 18–42, 102–125, 128–147). Imperial College Press.

[CHE2] Chen, S. H., & Feng, B. (2011). Size effect in micro-scale cantilever beam bending. *Acta Mechanica*, *219*(3-4), 291–307. doi:10.1007/s00707-011-0461-7

[CHE3] Cheng, L., Pan, M., Scofield, J., & Steckl, A. J. (2002). Growth and doping of SiC-thin films on low-stress, amorphous Si3N4/Si substrates for robust microelectromechanical systems applications. *Journal of Electronic Materials*, *31*(5), 361–365. doi:10.1007/s11664-002-0083-x

[DEB] Debelle, A., Thomé, L., Dompoint, D., Boulle, A., Garrido, F., Jagielski, J., & Chaussende, D. (2010). Characterization and modelling of the ion-irradiation induced disorder in 6H-SiC and 3C-SiC single crystals. *Journal of Physics D: Applied Physics*, *43*(45), 455408. doi:10.1088/0022-3727/43/45/455408

[DEV] Devanathan, R., Gao, F., & Weber, W. J. (2004). *Amorphization of silicon carbide by carbon displacement*. *Applied Physics Letters*, *84*(19), 3909. doi:10.1063/1.1739515

[FAN] Fang, W., Wickert, J.A. (1996). Determining mean and gradient residual stresses in thin films using micromachined cantilevers. *J. Micromech. Microeng.*, 6, 301-309.

[FRE1] Freund, L.B., Suresh, S. (2003). *Thin Film Materials: Stress, Defect Formation, and Surface Evolution* (pp. 15–83). Cambridge University Press.

[FRE2] Frewin, C. L., Locke, C., Wang, J., Spagnol, P., & Saddow, S. E. (2009). Growth of cubic silicon carbide on oxide using polysilicon as a seed layer for micro-electro-mechanical machine applications. *Journal of Crystal Growth*, *311*(17), 4179–4182. doi:10.1016/j.jcrysgro.2009.06.037

[FU1] Fu, X.-A., Dunning, J. L., Zorman, C. a., & Mehregany, M. (2005). Polycrystalline 3C-SiC thin films deposited by dual precursor LPCVD for MEMS applications. *Sensors and Actuators A: Physical*, *119*(1), 169–176. doi:10.1016/j.sna.2004.09.009

[FU2] Fu, X., Dunning, J. L., Zorman, C. a., & Mehregany, M. (2005). Measurement of residual stress and elastic modulus of polycrystalline 3C-SiC films deposited by low-pressure chemical vapor deposition. *Thin Solid Films*, *492*(1-2), 195–202. doi:10.1016/j.tsf.2005.07.236

[FU3] Fu, X.-A., Jezeski, R., Zorman, C. a., & Mehregany, M. (2004). Use of deposition pressure to control residual stress in polycrystalline SiC films. *Applied Physics Letters*, *84*(3), 341. doi:10.1063/1.1640781

[GAO1] Gao, D., Howe, R.T., Maboudian, R. (2003). Characterization of residual strain in SiC films deposited using 1,3-disilabutane for MEMS application. *JM^3,2(4), 259-264*

[GAO2] Gao, F., Chen, D., Hu, W., & Weber, W. J. (2010). Energy dissipation and defect generation in nanocrystalline silicon carbide. *Physical Review B*, *81*(18), 184101. doi:10.1103/PhysRevB.81.184101

[GAO3] Gao, F., & Weber, W. (2002). Cascade overlap and amorphization in 3C-SiC: Defect accumulation, topological features, and disordering. *Physical Review B*, *66*(2), 024106. doi:10.1103/PhysRevB.66.024106

[HAR] Harsha, K.S. Sree (2005). *Principles of vapor deposition of thin films*. Elsevier. pp. 685-829.

[HE] He, B. B. (2006). Measurement of Residual Stresses in Thin Films by Two-Dimensional XRD. *Materials Science Forum*, *524-525*, 613–618. doi:10.4028/www.scientific.net/MSF.524-525.613

[HOL] Hollauer, C. (2007). Modeling of Thermal Oxidation and Stress Effects. Technical University of Vienna. Retrieved from http://www.iue.tuwien.ac.at/phd/hollauer/node46.html#cantifig2

[INP] Inpg, L., & Galben, I. G. (2008). 3C-SiC growth on Si substrates via CVD : An introduction, (100), 1–8.

[ITO] Itoh, H., Yoshikawa, M., Nashiyama, I., Misawa, S., Okumura, H., & Yoshida, S. (1990). Radiation induced defects in CVD-grown 3C-SiC. *IEEE Transactions on Nuclear Science*, *37*(6), 1732–1738. doi:10.1109/23.101184

[JAN] Janssen, G. C. a. M. (2007). Stress and strain in polycrystalline thin films. *Thin Solid Films*, *515*(17), 6654–6664. doi:10.1016/j.tsf.2007.03.007

[JIA1] Jiang, L., Cheung, R., Hassan, M., Harris, a. J., Burdess, J. S., Zorman, C. a., & Mehregany, M. (2003). Fabrication of SiC microelectromechanical systems using one-step dry etching. *Journal of Vacuum Science & Technology B: Microelectronics and Nanometer Structures*, *21*(6), 2998. doi:10.1116/1.1627804

[JIA2] Jiang, L., Cheung, R., Hedley, J., Hassan, M., Harris, a. J., Burdess, J. S., Mehregany, M., et al. (2006). SiC cantilever resonators with electrothermal actuation. *Sensors and Actuators A: Physical*, *128*(2), 376–386. doi:10.1016/j.sna.2006.01.045

[KAT] Katoh, Y., Nozawa, T., Snead, L. L., Ozawa, K., & Tanigawa, H. (2011). Stability of SiC and its composites at high neutron fluence. *Journal of Nuclear Materials*, *417*(1-3), 400–405. doi:10.1016/j.jnucmat.2010.12.088

[KHA] Kahn, H., Ballarini, R., & Heuer, a. H. (2011). Thermal Expansion of Low-pressure Chemical Vapor Deposition Polysilicon Films. *Journal of Materials Research*, *17*(07), 1855–1862. doi:10.1557/JMR.2002.0274

[KIM] Kim, H.-J., Han, J.-H., Kaiser, R., Oh, K. H., & Vlassak, J. J. (2008). High-throughput analysis of thin-film stresses using arrays of micromachined cantilever beams. *The Review of scientific instruments*, *79*(4), 045112. doi:10.1063/1.2912826

[LIE] Lieberman, M.A., Lichtenberg, A.J. (1994). *Principles of Plasma Discharges and Materials Processing*. (pp. 327-404) Wiley & Sons

[LIU1] Liu, F., Carraro, C., Pisano, A. P., & Maboudian, R. (2010). Growth and characterization of nitrogen-doped polycrystalline 3C-SiC thin films for harsh environment MEMS applications. *Journal of Micromechanics and Microengineering*, *20*(3), 035011. doi:10.1088/0960-1317/20/3/035011

[LIU2] Liu, C. (2012). *Foundations of MEMS*. Pearson pp. 82-99, 353-371.

[MA] Ma, C.-H., Huang, J.-H., & Chen, H. (2002). Residual stress measurement in textured thin film by grazing-incidence X-ray diffraction. *Thin Solid Films*, *418*(2), 73–78. doi:10.1016/S0040-6090(02)00680-6

[MAD] Madapura, S., A.J. Steckl, and M. Loboda. (1999). "Heteroepitaxial Growth of SiC on Si(100) and (111) by Chemical Vapor Deposition Using Trimethylsilane." *Journal of the Electrochemical Society* 146(3), 1197-1202.

[MAI] Maier-Schneider, D., Koprululu, A., Ballhausen Holm, S. (1996). Elastic properties and microstructure of LPCVD polysilicon films. *Journal of Micromechanics and Microengineering*, *6*, 436–446.

[MAL] Malhotra, S., Rek, Z., Yalisove, S., & Bilello, J. (1997). Analysis of thin film stress measurement techniques. *Thin Solid Films*, *301*(1-2), 45–54. doi:10.1016/S0040-6090(96)09569-7

[MEH1] Mehregany, M., Matus, L. G., & Larkin, D. J. (1997). Internal stress and elastic modulus measurements on micromachined 3C-SiC thin films. *IEEE Transactions on Electron Devices*, *44*(1), 74–79. doi:10.1109/16.554795

[MEH2] Mehregany, M., Zorman, C. a., & Rajan, N. (1998). Silicon carbide MEMS for harsh environments. *Proceedings of the IEEE*, *86*(8), 1594–1609. doi:10.1109/5.704265

[NGO] Ngo, D., Feng, X., Huang, Y., Rosakis, a. J., & Brown, M. a. (2007). Thin film/substrate systems featuring arbitrary film thickness and misfit strain distributions. Part I: Analysis for obtaining film stress from non-local curvature information. *International Journal of Solids and Structures*, *44*(6), 1745–1754. doi:10.1016/j.ijsolstr.2006.10.016

[OHR] Ohring, M. (1992). The Materials Science of Thin Films. San Diego, CA: Academic Press.

[ROP] Roper, C.S., Howe, R.T., Maboudian, R. (2006). Stress control of polycrystalline 3C-SiC films in a large-scale LPCVD reactor using 1,3-disilabutane and dichlorosilane as precursors. *J. Micromech. Microeng.* 16, 2736-2739.

[ROY1] Roy, S., DeAnna, R. G., Zorman, C. a., & Mehregany, M. (2002). Fabrication and characterization of polycrystalline SiC resonators. *IEEE Transactions on Electron Devices*, *49*(12), 2323–2332. doi:10.1109/TED.2002.807445

[ROY2] Roy, S., Zorman, C., Mehregany, M., DeAnna, R., & Deeb, C. (2006). The mechanical properties of polycrystalline 3C-SiC films grown on polysilicon substrates by atmospheric pressure chemical-vapor deposition. *Journal of Applied Physics*, *99*(4), 044108. doi:10.1063/1.2169875

[SER] Serverino, A., C. Frewin, C. Bongiorno, R. Anzalone, S.E. Saddow, and F. La Via. (2009). Structural Defects in (100) 3C-SiC Heteroepitaxy: Influence of the Buffer Layer Morphology on Generation and Propagation of Stacking Faults and Microtwins. *Diamond & Related Materials* 18, 1440-1449.

[SHU] Shul, R.J., Pearton, S.J., Coburn, J.W., Stevens, J.E., Fleming, J. G. (2000). *Handbook of Advanced Plasma Processing Techniques*. (S. J. Shul, R.J., Pearton, Ed.) (pp. 1–31, 57–60, 419–425). Springer.

[SNE] Snead, L. L., Nozawa, T., Katoh, Y., Byun, T.-S., Kondo, S., & Petti, D. a. (2007). Handbook of SiC properties for fuel performance modeling. *Journal of Nuclear Materials*, *371*(1-3), 329–377. doi:10.1016/j.jnucmat.2007.05.016

[STA] Stanciu, S. G., Coltuc, D., Stanciu, G. A., Andreadou, A., Mantzari, A., & Polychroniadis, E. K. (2011). Automatic Estimation of Stacking Fault Density in SiC Specimens Imaged by Transmission Electron Microscopy, (111), 4–7.

[SWA] Swaminathan, N., Kamenski, P. J., Morgan, D., & Szlufarska, I. (2010). Effects of grain size and grain boundaries on defect production in nanocrystalline 3C–SiC. *Acta Materialia*, *58*(8), 2843–2853. doi:10.1016/j.actamat.2010.01.009

[WAN] Wang, C.-F., & Tsai, D.-S. (2000). Low pressure chemical vapor deposition of silicon carbide from dichlorosilane and acetylene. *Materials Chemistry and Physics*, *63*(3), 196–201. doi:10.1016/S0254-0584(99)00207-2

[WEB] Weber, W.J., Yu, N., Wang, L.M. (1998). Irradiation-induced amorphization in β-SiC. *Journal of Nuclear Materials.* 253, 53-59.

[WIJ] Wijesundara, M.B.J., Gao, D., Carraro, C., Howe, R.T., Maboudian, R. (2003). Nitrogen doping of polycrystalline 3C-SiC films grown using 1,3-disilabutane in a conventional LPCVD reactor. *Journal of Crystal Growth* 259, pp.18-25.

[WIT] Withers, P. J., & Bhadeshia, H. K. D. H. (2001). Residual stress. Part 2 – Nature and origins. *Materials Science and Technology*, *17*(4), 366–375. doi:10.1179/026708301101510087

[YUN] Yun, J., Takahashi, T., Ishida, Y., & Okumura, H. (2006). Dependence of stacking fault and twin densities on deposition conditions during 3C-SiC heteroepitaxial growth on on-axis Si(001) substrates. *Journal of Crystal Growth*, *291*(1), 140–147. doi:10.1016/j.jcrysgro.2006.03.005

[ZHA1] Zhang, J., Howe, R. T., & Maboudian, R. (2006). Control of strain gradient in doped polycrystalline silicon carbide films through tailored doping. *Journal of Micromechanics and Microengineering*, *16*(10), L1–L5. doi:10.1088/0960-1317/16/10/L01

[ZHA2] Zhang, Y., Ishimaru, M., Varga, T., Oda, T., Hardiman, C., Xue, H., Katoh, Y., et al. (2012). Nanoscale engineering of radiation tolerant silicon carbide. *Physical chemistry chemical physics : PCCP*, *14*(38), 13429–36. doi:10.1039/c2cp42342a

[ZHA3] Zhang, Y., Zhao, Y. (2005). An effective method of determining the residual stress gradients in a micro-cantilever. *Microsystem Technologies*, *12*(4), 357–364. doi:10.1007/s00542-005-0065-z

[ZOR] Zorman, C. a., Rajgopal, S., Fu, X. a., Jezeski, R., Melzak, J., & Mehregany, M. (2002). Deposition of Polycrystalline 3C-SiC Films on 100 mm Diameter Si(100) Wafers in a Large-Volume LPCVD Furnace. *Electrochemical and Solid-State Letters*, *5*(10), G99. doi:10.1149/1.1506461

APPENDIX

Appendix A – Description of Governing Cantilever Deflection Equations

The deflections in small scale devices resulting from the stress variation through the thickness of a thin-film material is a representation of the nonuniformities in the thin-film that occur during the deposition process. The bending moment which causes the deflection of a cantilever beam, for example originates from the pre-release residual stress and is given by,

$$M = \int_{-\frac{t}{2}}^{\frac{t}{2}} zb\sigma(z)\,dz \qquad \text{Eq.6}$$

where σ(z) represents the residual stress in the film as a function of film thickness, b is the cantilever width, and z is a relative position across the thickness of the film. If a linear strain gradient Γ is assumed the residual stress as a function of film thickness becomes,

$$\sigma(z) = E\Gamma z \qquad \text{Eq.7}$$

This converts Eq.7 and gives the following expression for the strain gradient,

$$\Gamma = \frac{M}{EI} \qquad \text{Eq.8}$$

where the moment of inertia, I, for a rectangular cross section is given by $I = bt^3/12$. Therefore Eq.8 above is given by the following after substitution and simplification,

$$\Gamma = \frac{12M}{Ebt^3} \qquad \text{Eq.9}$$

The measured vertical deflection, z, at the cantilever beam endpoint for a cantilever with an applied end moment is given as:

$$Z = \frac{ML^2}{2EI} = \frac{\Gamma L^2}{2} \qquad \text{Eq.10}$$

If the beam tip deflection is already known, then the strain gradient of the film can be calculated by rearranging Eq.10 above and solving directly using the following expression for the strain gradient:

$$\Gamma = \frac{2Z}{L^2} \qquad \text{Eq.11}$$

The relation of can be put in terms of stress by incorporating Young's modulus and is shown below in Eq. 12,

$$\Gamma\left(x = L\right) = \frac{2EZ}{L^2} \qquad \text{Eq.12}$$